On transformations and shape functions for enhanced assumed strain elements

Robin Pfefferkorn | Peter Betsch*

[1]Institute of Mechanics, Karlsruhe Institute of Technology (KIT), Germany

Correspondence

*Peter Betsch, Institute of Mechanics, Karlsruhe Institute of Technology, 76131 Karlsruhe, Germany. Email: peter.betsch@kit.edu

Summary

We summarize several previously published geometrically nonlinear EAS elements and compare their behavior. Various transformations for the compatible and enhanced deformation gradient are examined. Their effect on the patch test is one main concern of the work, and it is shown numerically and with a novel analytic proof, that the element proposed by Simo et al.[1] does not fulfill the patch test. We propose a modification to overcome that drawback without loosing the favorable locking-free behavior of that element. Furthermore, a new transformation for the enhanced field is proposed and motivated in a curvilinear coordinate frame. It is shown in numerical tests that this novel approach outperforms all previously introduced transformations.

KEYWORDS:

Mixed finite elements, Finite deformations, Enhanced assumed strains (EAS), Transformations, Hourglassing, Patch test

1 | INTRODUCTION

The computer simulation of large-scale solid mechanics problems requires robust, low-order and efficient general purpose finite elements. Such elements should be free of shear and volumetric locking, exhibit good coarse mesh accuracy and be insensitive to mesh distortion frequently induced by mesh generators (cf. Wriggers[2]). Additionally, no spurious (nonphysical) instabilities should arise from the element formulation. Unfortunately, low-order isoparametric displacement elements do not meet all of these criteria and show e.g. severe locking in bending dominated problems as well as in the incompressible limit. Thus, there is a long history of various *mixed methods*, which incorporate extra fields such as strains or stresses as primary variables in addition to the displacements.

A particular class of widely used mixed elements is based on the *enhanced assumed strain* (EAS) method, which was introduced for linear kinematics by Simo and Rifai[3] and for nonlinear kinematics by Simo and Armero[4] in the early 1990s. It is based on a *Hu-Washizu* type variational functional (cf.[5]) and its key idea is to introduce an enhanced strain field in addition to the compatible strains computed from the displacement field. This facilitates greatly reduced locking both in the nearly incompressible limit and in bending dominated problems[1]. The EAS method gives a mathematically solid foundation for the earlier introduced popular incompatible mode model by Wilson et al.[8], which was further improved by Taylor et al.[9] to pass the patch test. Note, that the element presented by Taylor et al.[9] is a special case of an EAS element. Moreover, all EAS-elements can be expressed as incompatible mode elements with the more complex scheme developed by Bischoff and Romero[10].

The EAS method provides a framework to construct finite elements with many desired properties. They can be constructed completely locking free, are relatively insensitive to mesh distortion, exhibit good coarse mesh accuracy and nonlinear material laws

---

[1]Note, that there is a limit to improving the bending behavior in distorted meshes as shown by MacNeal[6,7]

can easily be implemented due to the strain driven format. Thus, there is a plethora of publications on the method in various fields such as shell structures, modeling of failure and even diffusion problems (e.g. [11,12,13,14,15,16]). In the present work, however, focus is put on 2D and 3D nonlinear solid mechanics (e.g. [4,1,17,18,12,19,20,21,22,23,24,25,26,27,28,29,30,31,32,33,34,35,36,37] among others).

As mentioned above, the first geometrically nonlinear EAS element was proposed by Simo and Armero[4]. It is based on an enhancement of the deformation gradient and uses the nine (in 3D) *Wilson-modes* as shape functions for the enhanced deformation gradient. This element was then improved by Simo et al.[1] with three additional enhanced modes and a modification of the compatible deformation gradient to get a completely locking free element, which is important especially in elasto-plastic simulations as shown by Andelfinger et al.[38]. Unfortunately, the element presented in [1] does not fulfill the patch test (cf.[21,34]). This issue will be thoroughly addressed in the present work. Another completely locking free element with a total of 21 enhanced modes, that passes the patch test was introduced by Andelfinger and Ramm[13]. A disadvantage of approaches using that many enhanced modes is the limited convergence radius of Newton's method due to the higher number of degrees of freedom from the higher order enhanced modes.

However, the probably most important drawback of the EAS method are nonphysical instabilities, which were already mentioned in the very first publication of Simo and Armero[4]. Interestingly, these instabilities arise only in the geometrically nonlinear case. In the linear case, the EAS method does not exhibit nonphysical instabilities, if three simple requirements are met (cf.[3,39,40]). However, the first nonlinear EAS element presented by Simo and Armero[4] exhibits an hour-glassing instability under compression regardless of the material model used. This was first thoroughly covered and examined by Wriggers and Reese[41], Reese[42] for a Neo-Hookean material and de Souza Neto et al.[43] for elasto-plasticity. These works showed that hour-glassing occurs in a simple one element test case. More recently, Sussman and Bathe[37] showed, that these instabilities arise even in states of small strains, if the geometric aspect ratio of the elements is large. This renders EAS elements based on Wilson-modes almost unusable.

Thus, there have been many attempts to cure the instability, but none of which has proven to solve all problems so far. A first approach was presented by Korelc and Wriggers[19], whose element was adapted for objectivity by Glaser and Armero[22]. They proposed using the transpose of the Wilson-modes as shape functions for the enhanced deformation gradient and showed that the resulting element is free of spurious instabilities at least for the considered hyperelastic material. Unfortunately, for elasto-plastic and unstable elastic materials (see[22]) it still exhibits spurious hour-glassing modes (see Armero[26]). Note, that the linearization of both, the modified element[22] and the standard EAS element based on Wilson modes[4], yields the same geometrically linear EAS element[3].

Further attempts to remove the instability have e.g. been conducted in [26,18,22,29,44,30,45,35]. The elements of Glaser and Armero[22] and Korelc et al.[35] rely on the transpose Wilson-modes, with further modifications, such as Taylor-expansion of the shape functions (see[20,24]) in case of the element by Korelc et al.[35]. These elements are still not completely hour-glassing free unless additional stabilization terms with arbitrary stabilization parameters are introduced. Such artificial stabilization techniques are also used by e.g. Reese and Wriggers[29], Reese[44], Wall et al.[30] and Areias et al.[45]. The latter work uses a penalty form of the usual variational framework for the EAS method. This penalty term has to be activated if hour-glassing arises but then predates the benefits of the EAS method. Armero[26] introduced a combination of the EAS method by Glaser and Armero[22] with the mixed pressure element by Simo et al.[46]. The formulation further improves stability of the element by[22] but does not yield an unconditionally stable element (cf.[26]). Crisfield et al.[18] proposed enhancing the right stretch tensor instead of the deformation gradient which yields a very complex formulation due to the needed co-rotational finite element framework and seems to induce locking in some cases (see[2]). Another attempt made by Müller-Hoeppe et al.[34] splits the deformation into an homogeneous and inhomogeneous part. The instability is then removed by applying geometric nonlinear enhancement only to the homogeneous part and treating the enhancement of the inhomogeneous one with methods from linear theory. Apart from being nonphysical, major problems arise in the construction of material models for the method. A final possibility is to remove some critical enhancement modes as done e.g. by Krischok and Linder[16], but this method removes the beneficial effects of those modes as well. Thus, it must be a case to case decision, if these modes are necessary to retain an efficient EAS element. All in all, there is so far no unconditionally stable EAS element without other major drawbacks.

The purpose of the present work is to summarize and compare shape functions and transformations previously used for EAS elements. One principal point is the modification of the compatible deformation gradient presented by Simo et al.[1], which leads to a violation of the patch test in generally distorted meshes (see[21,34]). In the present work, we show that this failure can be cured with a simple modification which stems from the hourglass-stabilization introduced by Flanagan and Belytschko[47].We provide numerical and more importantly analytic proof, that the patch test is fulfilled by the newly developed approach. Furthermore, a

new transformation between the reference and physical frame is proposed for the enhanced deformation gradient. This transformation is motivated with the help of a curvilinear coordinate system. Numerical investigations show the superior behavior of the novel approach compared to previously used formulas.

The present work is structured as follows. Section 2 briefly reviews the geometrically nonlinear EAS method and different approaches used within that framework. Focus is for that matter put on the finite element approximation of the compatible and enhanced deformation gradient in Section 2.2 and the patch test in Section 2.4. Details about the curvilinear framework to derive the novel transformation approach are given in Appendix A. Additional information on computations needed to fix the violation of the patch test by the element of Simo et al.[1] is given in Appendix B. Furthermore, Appendix C covers the analytic proof, that the newly proposed improved version of the modification of Simo et al.[1] passes the patch test for arbitrarily distorted meshes. Numerical investigations to examine the properties of the elements introduced in Section 2 are given in Section 3, where standard benchmarks are used to assess the elements. Finally, a conclusion summarizes the work in Section 4.

2 | ENHANCED ASSUMED STRAIN METHOD

This section briefly reviews the framework of the *EAS-method* for nonlinear kinematics, which was first presented by Simo and Armero[4]. Focus is put on the *finite-element* approximations of the deformation gradient. Various transformations for the compatible and incompatible field (see e.g. [3,1,22,16]) are summarized and partly motivated with the help of a *curvilinear* coordinate system. Furthermore, novel transformations are introduced for both parts of the deformation gradient.

2.1 | Variational framework

The motion of a deformable body from its reference configuration $\mathcal{B}_0 \in \mathbb{R}^3$ to its current configuration $\mathcal{B} \in \mathbb{R}^3$ is described by a bijective deformation map $\boldsymbol{\varphi} : \mathcal{B}_0 \to \mathbb{R}^3$, which maps material points $\mathbf{X} \in \mathcal{B}_0$ onto spatial points $\mathbf{x} := \boldsymbol{\varphi}(\mathbf{X}) \in \mathcal{B}$. On a portion $\partial_\varphi \mathcal{B}_0$ of the boundary $\partial \mathcal{B}_0$ the displacements are prescribed by $\bar{\boldsymbol{\varphi}} : \partial_\varphi \mathcal{B}_0 \to \mathbb{R}^3$. Altogether the deformation map is given by

$$\boldsymbol{\varphi} \in \mathcal{U} = \left\{ \boldsymbol{\varphi} : \mathcal{B}_0 \to \mathbb{R}^3 \,\Big|\, (\boldsymbol{\varphi})_i \in H_1, \ \det(\mathrm{D}\boldsymbol{\varphi}) > 0 \text{ and } \boldsymbol{\varphi}(\mathbf{X}) = \bar{\boldsymbol{\varphi}}(\mathbf{X}), \mathbf{X} \in \partial_\varphi \mathcal{B}_0 \right\}. \tag{1}$$

The key idea of the geometrically nonlinear EAS method first presented by Simo and Armero[4] is to recast the deformation gradient $\mathbf{F}(\mathbf{X})$ at a material point $\mathbf{X}$ into the form

$$\mathbf{F}(\mathbf{X}) = \mathbf{F}_\varphi(\boldsymbol{\varphi}) + \tilde{\mathbf{F}}(\boldsymbol{\varphi}, \boldsymbol{\alpha}), \tag{2}$$

where $\mathbf{F}_\varphi = \partial \boldsymbol{\varphi}/\partial \mathbf{X} = \mathrm{D}\boldsymbol{\varphi}(\mathbf{X})$ and $\tilde{\mathbf{F}}(\boldsymbol{\varphi}, \boldsymbol{\alpha})$[2] represent the compatible and enhanced part of the deformation gradient, respectively. Furthermore, the enhanced deformation gradient

$$\tilde{\mathbf{F}}(\boldsymbol{\varphi}, \boldsymbol{\alpha}) \in \tilde{\mathcal{F}} = \left\{ \tilde{\mathbf{F}} : \mathcal{B}_0 \to \mathbb{R}^{3\times3} \,\Big|\, (\tilde{\mathbf{F}})_{ij} \in L_2 \right\} \tag{3}$$

is introduced as function of the deformation $\boldsymbol{\varphi} \in \mathcal{U}$ and n_{enh} enhanced parameters α_i, $i = 1, \ldots, n_{enh}$ arranged in vector $\boldsymbol{\alpha} \in \left\{ \boldsymbol{\alpha} : \mathcal{B}_0 \to \mathbb{R}^{n_{enh}} | \alpha_i \in L_2 \right\}$.

Remark 1. Enhancing the deformation gradient (2) is not the only possible form of enhancement. Other kinematic measures can be enhanced analogously. Refer to e.g. [30,48,12,49,23] (enhancement of the *Green-Lagrange-Strains*) and [18] (enhancement of the *right stretch tensor* combined with *co-rotational* approach).

Remark 2. Note, that the dependence of $\tilde{\mathbf{F}}$ (3) on $\boldsymbol{\varphi}$ and $\boldsymbol{\alpha}$ is a general case employed e.g. in [22,1] and can be simplified significantly, if the enhanced field can be derived from an incompatible displacement field (see Section 2.2.2 and [1]).

Definitions (1) and (3) enable to give the *Hu-Washizu*-type *variational functional* of the EAS method for a hyperelastic material with *polyconvex strain-energy-function* $\mathbb{W}(\mathbf{F})$ through

$$\Pi_{\mathrm{EAS}}(\boldsymbol{\varphi}, \tilde{\mathbf{F}}, \mathbf{P}) = \int_{\mathcal{B}_0} \mathbb{W}(\mathbf{F}) - \mathbf{P} : \tilde{\mathbf{F}} \, \mathrm{d}V + \Pi_{\mathrm{ext}}(\boldsymbol{\varphi}), \tag{4}$$

---

[2]Note that subsequently arguments of functions are often omitted in favor of readability and notational simplicity.

where $\Pi_{\text{ext}}(\boldsymbol{\varphi})$ denotes the potential of external forces not further specified here (cf.[4]). The third argument of Π_{EAS}, namely $\mathbf{P}$, is a stress-like variable and can be interpreted as *Lagrange multiplier* ensuring that condition $\tilde{\mathbf{F}} = \mathbf{0}$ holds in a continuous setting. It is defined as

$$\mathbf{P} \in \mathcal{P} = \left\{ \mathbf{P} \, : \, \mathcal{B}_0 \to \mathbb{R}^{3\times3} \, \middle| (\mathbf{P})_{ij} \in L_2 \right\}. \tag{5}$$

The stationary conditions of (4) with respect to $\boldsymbol{\varphi} \in \mathcal{U}$, $\tilde{\mathbf{F}} \in \tilde{\mathcal{F}}$ and $\mathbf{P} \in \mathcal{P}$ are given in a next step. The corresponding admissible variations are $\delta\boldsymbol{\varphi} \in \mathcal{V}$, $\delta\tilde{\mathbf{F}} \in \tilde{\mathcal{F}}$ and $\delta\mathbf{P} \in \mathcal{P}$, where the set of admissible variations for the deformation $\boldsymbol{\varphi}$ has the form

$$\mathcal{V} = \left\{ \boldsymbol{\varphi} \, : \, \mathcal{B}_0 \to \mathbb{R} \, \middle| (\boldsymbol{\varphi})_i \in H_1 \text{ and } \boldsymbol{\varphi}(\mathbf{X}) = \mathbf{0}, \mathbf{X} \in \partial_\varphi \mathcal{B}_0 \right\}. \tag{6}$$

Since $\tilde{\mathbf{F}}$ was introduced as function of $\boldsymbol{\varphi}$ and $\boldsymbol{\alpha}$ in (3), it is straightforward to show, that relation

$$\delta\tilde{\mathbf{F}} = \delta_\varphi \tilde{\mathbf{F}} + \delta_\alpha \tilde{\mathbf{F}} \tag{7}$$

holds. Therein $\delta_{(\bullet)}$ denotes the first variation of a functional with respect to $(\bullet)$. With this information at hand, the stationary conditions of (4) read

$$\delta_\varphi \Pi_{\text{EAS}} = \int_{\mathcal{B}_0} \hat{\mathbf{P}} : \delta_\varphi \mathbf{F} - \mathbf{P} : \delta_\varphi \tilde{\mathbf{F}} \, \mathrm{d}V + \delta_\varphi \Pi_{\text{ext}} = 0, \tag{8a}$$

$$\delta_\alpha \Pi_{\text{EAS}} = \int_{\mathcal{B}_0} \hat{\mathbf{P}} : \delta_\alpha \mathbf{F} - \mathbf{P} : \delta_\alpha \tilde{\mathbf{F}} \, \mathrm{d}V = 0, \tag{8b}$$

$$\delta_\mathbf{P} \Pi_{\text{EAS}} = - \int_{\mathcal{B}_0} \delta\mathbf{P} : \tilde{\mathbf{F}} \, \mathrm{d}V = 0, \tag{8c}$$

where $\hat{\mathbf{P}} = \partial_\mathbf{F} \mathbb{W}(\mathbf{F})$ denotes the constitutive stress tensor.

Remark 3. Note, that (8c) implies $\tilde{\mathbf{F}} = \mathbf{0}$ on body $\mathcal{B}_0$ in a continuous setting, which is ensured by *Lagrange multiplier* $\mathbf{P}$. Inserting $\tilde{\mathbf{F}} = \mathbf{0}$ into (8a) and (8b) reduces (8) to a pure displacement formulation showing consistency with continuum mechanics. However, this result holds only in a continuous, non-discrete setting. Using (8) as basis for a FE approximation can lead to improved numerical results.

Remark 4. Usually[3,4], (8) is simplified by requiring L_2-orthogonality between the Lagrange-multipliers $\mathbf{P}$ and the enhanced deformation gradient $\tilde{\mathbf{F}}$ in a discrete setting. This makes the corresponding terms vanish in the equations above. For more details refer to Section 2.3.

2.2 | Finite element approximations

The *finite element method* (FEM) is one way to get an approximate solution of (8). In the present work only 4-node quadrilateral (2D) and 8-node brick (3D) elements Ω_e are considered for the discretization of body $\mathcal{B}$. The corresponding reference elements $\hat{\Omega} = [-1, 1]^{n_{dim}}$ are a bi-unit square and cube, respectively. Subsequently, focus is put on shape functions etc. for the 3D case. They can however, easily be reduced to 2D equivalents.

2.2.1 | Compatible deformation gradient

In this Section we introduce several procedures to compute the compatible deformation gradient. Firstly we briefly present the well-known isoparametric concept which is also the standard procedure used for EAS elements (cf.[4]). Secondly, we present a modification to that concept introduced by Simo et al.[1] which improves the locking behavior of the elements but leads to a violation of the patch test (cf.[21,34,45]). Finally, a new approach is presented which cures the failure of the patch test due to the modification of Simo et al.[1] but maintains its favorable locking behavior.
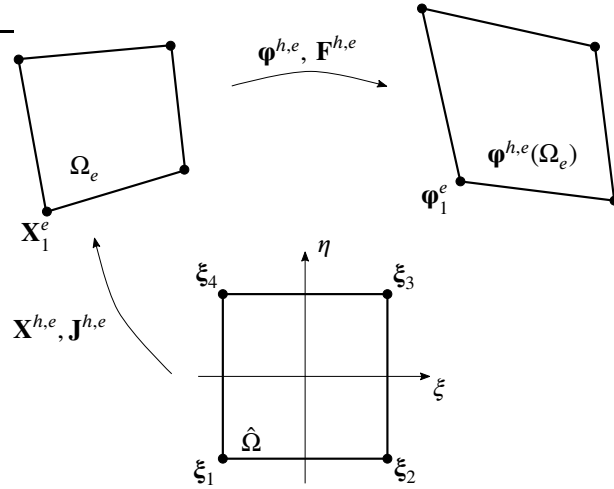
FIGURE 1 Isoparametric map of a quadrilateral 2D finite element Ω_e

The standard procedure

Geometry and deformation are approximated[3] using the standard *isoparametric* concept (cf.[2,50] for details). Thus,

$$\mathbf{X}^{h,e} = \sum_{I=1}^{8} N_I(\boldsymbol{\xi})\mathbf{X}_I^e, \qquad \boldsymbol{\varphi}^{h,e} = \sum_{I=1}^{8} N_I(\boldsymbol{\xi})\boldsymbol{\varphi}_I^e, \tag{9}$$

is defined for the approximations of geometry $\mathbf{X}$ and deformation $\boldsymbol{\varphi}$ within one finite element Ω_e. Therein, $\mathbf{X}_I^e$ and $\boldsymbol{\varphi}_I^e$ denote the nodal reference coordinates and deformation, respectively. Furthermore, standard *tri-linear* shape functions for the bi-unit cube with vertices (ξ_I, η_I, ζ_I) are employed. They are specified by

$$N_I(\boldsymbol{\xi}) = \frac{1}{8}(1 + \xi_I\xi)(1 + \eta_I\eta)(1 + \zeta_I\zeta), \quad I = 1, \dots, 8, \tag{10}$$

and defined on the reference element $\hat{\Omega}$ in coordinate system $\boldsymbol{\xi} = [\xi, \eta, \zeta]^{\mathrm{T}}$. The variations $\delta\boldsymbol{\varphi}$ are approximated in the same way as $\boldsymbol{\varphi}$ in (9) yielding

$$\boldsymbol{\varphi}^h \in \mathcal{U}^h = \left\{ \boldsymbol{\varphi}^h \in \mathcal{U} \,\middle|\, \boldsymbol{\varphi}^h = \sum_{e=1}^{n_{el}} \boldsymbol{\varphi}^{h,e} \quad \text{and} \quad \boldsymbol{\varphi}_I^e(\mathbf{X}_I^e) = \bar{\boldsymbol{\varphi}}^{h,e}, \ \mathbf{X}_I^e \in \partial_{\varphi}\mathcal{B}_0^{h,e} \right\}, \tag{11}$$

$$\delta\boldsymbol{\varphi}^h \in \mathcal{V}^h = \left\{ \delta\boldsymbol{\varphi}^h \in \mathcal{V} \,\middle|\, \delta\boldsymbol{\varphi}^h = \sum_{e=1}^{n_{el}} \delta\boldsymbol{\varphi}^{h,e} \quad \text{and} \quad \delta\boldsymbol{\varphi}_I^e(\mathbf{X}_I^e) = \mathbf{0}, \ \mathbf{X}_I^e \in \partial_{\varphi}\mathcal{B}_0^{h,e} \right\}, \tag{12}$$

for the discrete ansatz spaces of the deformation and variations thereof (cf.[2]).

With this information at hand, transformations between the reference element and material configuration of a finite element Ω_e (see Fig. 1) can be described by

$$\mathbf{J}^{h,e} = \frac{\partial\mathbf{X}^{h,e}}{\partial\boldsymbol{\xi}} = \sum_{I=1}^{8} \mathbf{X}_I^e \otimes \nabla_{\boldsymbol{\xi}} N_I, \tag{13a}$$

$$j^{h,e} = \det(\mathbf{J}^{h,e}), \tag{13b}$$

which denote the *Jacobian* matrix $\mathbf{J}^{h,e}$ of the transformation and its determinant $j^{h,e}$, respectively (cf.[2,3]). Finally, the approximation of the compatible part $\mathbf{F}_{\varphi}$ of the deformation gradient (2) is given by

$$\mathbf{F}_{\varphi}^{h,e} = \mathrm{D}\boldsymbol{\varphi}^{h,e} = \frac{\partial\boldsymbol{\varphi}^{h,e}}{\partial\mathbf{X}^{h,e}} = \sum_{I=1}^{8} \boldsymbol{\varphi}_I^e \otimes \nabla_{\mathbf{X}} N_I, \tag{14}$$

---

[3] Approximations are denoted by superscript h.

where the derivatives of the shape functions with respect to $\mathbf{X}$ can be computed via well-known relation

$$\nabla_{\mathbf{X}} N_I = (\mathbf{J}^{h,e})^{-T} \nabla_{\boldsymbol{\xi}} N_I. \tag{15}$$

Modification of the compatible deformation gradient by Simo et al.

Simo et al.[1] proposed a modified formula for the compatible deformation gradient to be used instead of (14). It allows to completely eliminate locking but unfortunately leads to violation of the patch test (see Sections 2.4 and 3.1, Appendix C as well as references[21,34,45]). Nevertheless, the modification of the conforming deformation gradient is presented here to complete the overview of approximations for EAS elements. The idea proposed by Simo et al.[1] is to evaluate the gradients of the shape functions analogously to the enhanced field (see Section 2.2.2) and is based on a different representation of the shape functions used frequently for hourglass-stabilization (see e.g.[51]). It ultimately leads to a modified gradient

$$\widetilde{\nabla}_{\mathbf{X}} N_I = \nabla_{\mathbf{0}} N_I + \sum_{A=1}^{4} \frac{j_0}{j^{h,e}} \mathbf{J}_0^{-T} \nabla_{\boldsymbol{\xi}} H_A \gamma_I^A, \qquad I = 1, \dots, 8. \tag{16}$$

of the shape functions, which is then used in (14) instead of (15) to compute the conforming deformation gradient $\mathbf{F}_\varphi^{h,e}$. In the last equation,

$$\nabla_{\mathbf{0}} N_I := \nabla_{\mathbf{X}} N_I|_{\boldsymbol{\xi}=\mathbf{0}}, \tag{17}$$

$$\mathbf{J}_0 := \mathbf{J}^{h,e}(\boldsymbol{\xi}=\mathbf{0}) \quad \text{and} \quad j_0 := j^{h,e}(\boldsymbol{\xi}=\mathbf{0}), \tag{18}$$

are the evaluations at the element centroid ($\boldsymbol{\xi} = \mathbf{0}$) of (13) and (15). Moreover, $\nabla_{\boldsymbol{\xi}} H_A$, $A = 1, \dots, 4$ are derivatives of the four *hourglass functions*

$$H_1 = \eta\zeta, \quad H_2 = \xi\zeta, \quad H_3 = \xi\eta, \quad H_4 = \xi\eta\zeta, \tag{19}$$

and γ_I^A are the components of the *gamma stabilization* vectors given by

$$\boldsymbol{\gamma}^A = \frac{1}{8} \left[\mathbf{h}^A - (\nabla_{\mathbf{0}} \mathbf{N})^{T} \tilde{\mathbf{X}}^e \mathbf{h}^A \right], \qquad A = 1, \dots, 4, \tag{20}$$

where

$$\nabla_{\mathbf{0}} \mathbf{N} = \left[\nabla_{\mathbf{0}} N_1 \;\; \cdots \;\; \nabla_{\mathbf{0}} N_8 \right], \tag{21}$$

$$\tilde{\mathbf{X}}^e = \left[\mathbf{X}_1^e \;\; \cdots \;\; \mathbf{X}_8^e \right], \tag{22}$$

$$\mathbf{h}^1 = \left[\begin{array}{cccccccc} 1 & 1 & -1 & -1 & -1 & -1 & 1 & 1 \end{array} \right]^{T},$$

$$\mathbf{h}^2 = \left[\begin{array}{cccccccc} 1 & -1 & -1 & 1 & -1 & 1 & 1 & -1 \end{array} \right]^{T},$$

$$\mathbf{h}^3 = \left[\begin{array}{cccccccc} 1 & -1 & 1 & -1 & 1 & -1 & 1 & -1 \end{array} \right]^{T}, \tag{23}$$

$$\mathbf{h}^4 = \left[\begin{array}{cccccccc} -1 & 1 & -1 & 1 & 1 & -1 & 1 & -1 \end{array} \right]^{T}.$$

Refer to[1] for a more detailed description of the modifications.

Remark 5. Note, that the standard gradients of the tri-linear shape functions given by (15) are obtained in the context of this alternative notation by using

$$\nabla_{\mathbf{X}} N_I = \nabla_{\mathbf{0}} N_I + \sum_{A=1}^{4} (\mathbf{J}^{h,e})^{-T} \nabla_{\boldsymbol{\xi}} H_A \gamma_I^A, \qquad I = 1, \dots, 8. \tag{24}$$

instead of (16). Thus, the modification presented by[1] is established by replacing $(\mathbf{J}^{h,e})^{-T}$ in the original formulation (24) with $\frac{j_0}{j^{h,e}} \mathbf{J}_0^{-T}$. We stress once more, that this modification leads to a violation of the patch test for distorted 3D meshes, which is shown numerically in Section 3.1 and analytically in Appendix C.

Remark 6. In 2D, there is only one hourglass-function $H_1 = \xi\eta$ with corresponding vector $\mathbf{h_1} = \left[1 \;\; -1 \;\; 1 \;\; -1 \right]^{T}$ and *gamma-stabilization* vector

$$\boldsymbol{\gamma}^1 = \frac{1}{4} \left[\mathbf{h}^1 - (\nabla_{\mathbf{0}} \mathbf{N})^{T} \tilde{\mathbf{X}}^e \mathbf{h}^1 \right]. \tag{25}$$

Furthermore, gradient (15) and (16) are always identical in 2D, which is also stated in [1]. This can be verified by comparing (16) and (24), which leaves

$$j^{h,e}(\mathbf{J}^{h,e})^{-\mathrm{T}}\nabla_{\boldsymbol{\xi}}(H_1) = j_0\mathbf{J}_0^{-\mathrm{T}}\nabla_{\boldsymbol{\xi}}(H_1) \tag{26}$$

to prove. The last equation can be established with lengthy but basic steps.

Improved version of the modification by Simo et al.

Finally, we present a new version to compute the compatible deformation gradient. It is based on the modification introduced by Simo et al. [1] (see above) and maintains its favorable locking behavior whilst curing the violation of the patch test. The only modification necessary is to replace $\nabla_{\mathbf{0}}N_I$ in (16) and (20) with

$$\bar{\nabla}_{\mathbf{X}}N_I = \frac{1}{V}\int_{\Omega_e}\nabla_{\mathbf{X}}N_I\,\mathrm{d}V, \qquad I = 1,\dots,8 \tag{27}$$

which is the average of the gradient of the shape functions within an element Ω_e with volume V. It can be evaluated efficiently with an analytic method developed by Flanagan and Belytschko [47], which is summarized in Appendix B of the present work. The idea of using (27) stems from the works of Flanagan and Belytschko [47] and Belytschko et al. [51] and is well-known to cure the violation of the patch test in the context of hourglass-stabilization (see also [52,53]). However, it has to the best of our knowledge[4] not been used for EAS elements so far. In Appendix C we show analytically, that the proposed approach fulfills the patch test for arbitrarily distorted meshes in the present EAS framework.

The compatible deformation gradient is finally computed by using again (14) and replacing the standard gradient of shape functions $\nabla_{\mathbf{X}}N_I$ used there with

$$\hat{\nabla}_{\mathbf{X}}N_I = \bar{\nabla}_{\mathbf{X}}N_I + \sum_{A=1}^{4}\frac{j_0}{j^{h,e}}\mathbf{J}_0^{-\mathrm{T}}\nabla_{\boldsymbol{\xi}}H_A\hat{\gamma}_I^A, \qquad I = 1,\dots,8, \tag{28}$$

where the modified gamma-stabilization vectors are given by

$$\hat{\boldsymbol{\gamma}}^A = \frac{1}{8}\left[\mathbf{h}^A - (\bar{\nabla}_{\mathbf{X}}\mathbf{N})^{\mathrm{T}}\tilde{\mathbf{X}}^e\mathbf{h}^A\right]. \tag{29}$$

Remark 7. Without the modifications with the center evaluation of the Jacobian (see Remark 5), (28) is given by

$$\hat{\nabla}_{\mathbf{X}}N_I = \bar{\nabla}_{\mathbf{X}}N_I + \sum_{A=1}^{4}(\mathbf{J}^{h,e})^{-\mathrm{T}}\nabla_{\boldsymbol{\xi}}H_A\hat{\gamma}_I^A, \qquad I = 1,\dots,8. \tag{30}$$

Note, that this is in contrast to (24) not equivalent to the standard gradient of shape functions (15), since a part of the shape functions is omitted as shown in Appendix B. However, this has no negative implications on neither the accuracy of the method nor the completeness of the approximation spaces (see also Appendix B and Belytschko and Bindemann [52]). On the contrary it provides the major advantage that it enables fulfilling the patch test for arbitrarily distorted meshes (see Appendix C).

2.2.2 | Enhanced deformation gradient

After having described the approximation of the compatible part $\mathbf{F}_{\varphi}$ of the deformation gradient (2) in the last section, focus is now put on the approximation of the enhanced part $\tilde{\mathbf{F}}$. We list various requirements and review a general framework for a wide range of shape functions first presented by [1] (see also [22]).

The first requirement is *frame invariance*. By considering a superposed rigid body motion $\boldsymbol{\varphi}^* = \mathbf{Q}\boldsymbol{\varphi} + \mathbf{c}$ with the constant vector $\mathbf{c} \in \mathbb{R}^3$ and rotation matrix $\mathbf{Q} \in \mathrm{SO}(3)$ we note that the conforming deformation gradient $\mathbf{F}_{\varphi}$ transforms according to rule $\mathbf{F}_{\varphi}(\boldsymbol{\varphi}^*) = \mathbf{Q}\mathbf{F}_{\varphi}(\boldsymbol{\varphi})$. To get an overall *frame invariant* method, it is necessary that the complete deformation gradient (2) transforms accordingly. This ultimately yields requirement

$$\tilde{\mathbf{F}}(\boldsymbol{\varphi}^*, \boldsymbol{\alpha}) = \mathbf{Q}\tilde{\mathbf{F}}(\boldsymbol{\varphi}, \boldsymbol{\alpha}) \tag{31}$$

for the *incompatible* part of the deformation gradient. Usually, the incompatible part is approximated element-wise, to enable *static condensation* of the additional *degrees of freedom* and to get an efficient element. A possible and frequently used structure

---

[4]During the review process we have been made aware of a similar but more complicated method proposed by Areias et al. [45].

for the enhanced part of the deformation gradient is

$$\tilde{\mathbf{F}}^h \in \tilde{\mathcal{F}}^h = \left\{ \tilde{\mathbf{F}}^h \in \tilde{\mathcal{F}} \;\middle|\; \tilde{\mathbf{F}}^h = \sum_{e=1}^{n_{el}} \chi_e \tilde{\mathbf{F}}^h(\boldsymbol{\varphi}, \boldsymbol{\alpha}) = \sum_{e=1}^{n_{el}} \chi_e \mathbf{T}_0(\boldsymbol{\varphi}) \bar{\mathbf{F}}^e(\boldsymbol{\alpha}) \right\}, \tag{32}$$

which was first presented by Simo et al. [1] and is an element-wise approximation since

$$\chi_e = \begin{cases} 1, & \mathbf{X} \in \Omega_e \\ 0, & \text{else} \end{cases}. \tag{33}$$

The tensor $\mathbf{T}_0$ ensures frame invariance according to (31) if condition $\mathbf{T}_0(\boldsymbol{\varphi}^*) = \mathbf{Q}\mathbf{T}_0(\boldsymbol{\varphi})$ holds. Furthermore, $\mathbf{T}_0$ has to be element-wise constant in order to fulfill the patch test (see Section 2.4). A simple way to satisfy these conditions is setting

$$\mathbf{T}_0 = \mathbf{F}_0 := \mathrm{D}\boldsymbol{\varphi}^{h,e}|_{\boldsymbol{\xi}=\mathbf{0}} = \mathbf{F}_\varphi^{h,e}(\boldsymbol{\xi} = \mathbf{0}) \tag{34}$$

which corresponds to evaluation of the conforming deformation gradient (14) at the element centroid (cf. [1]). However, other measures can be used. One novel version introduced in the present work employs the transposed inverse of $\mathbf{F}_0$ in the form

$$\mathbf{T}_0 = \mathbf{F}_0^{-\mathrm{T}}, \tag{35}$$

which is motivated in Appendix A. It can easily be shown, that this choice of $\mathbf{T}_0$ fulfills the aforementioned requirements. Further possibilities used in previous publications are given in Remark 8.

Remark 8. The center evaluation (34) is e.g. used in [1,22,35,26]. A possible alternative is the use of the average deformation gradient

$$\mathbf{F}_{avg} = \frac{1}{V} \int_{\Omega_e} \mathbf{F}^{h,e} \, \mathrm{d}V \tag{36}$$

within an element with volume V as done in e.g. [28,16,15,34]. However, differences between using the average value and the evaluation at the element centroid are very small in usual problems without localization of strains (see Section 3.7). Other alternatives used in previous publications are the co-rotational approach using the rotation tensor $\mathbf{R}$ at the element centroid emerging from the polar decomposition of the deformation gradient $\mathbf{F}$ (cf. [18] - enhancement is applied to the *right stretch tensor* instead of the deformation gradient in that work).

The last part of the deformation gradient (2), that needs to be approximated is the part $\bar{\mathbf{F}}^e$ introduced in (32). According to Glaser and Armero [22], a general form for arbitrary shape functions is given by

$$\bar{\mathbf{F}}^e = \sum_{I=1}^{n_{enh}} \mathbf{M}_I(\mathbf{X})\alpha_I, \tag{37}$$

where α_I are the n_{enh} enhanced parameters per element and $\mathbf{M}_I$ are the transformed shape functions. However, there are many possible transformations of the shape functions $\hat{\mathbf{M}}_I(\boldsymbol{\xi})$ defined on the reference element $\hat{\Omega}$ to the physical space. In general, they improve the bending behavior in initially distorted meshes. One well-working and widely used possibility (cf. e.g. [22,26,27,28,16,19]) is

$$\mathbf{M}_I(\mathbf{X}) = \frac{j_0}{j^{h,e}(\boldsymbol{\xi})} \mathbf{J}_0^{-\mathrm{T}} \hat{\mathbf{M}}_I(\boldsymbol{\xi}) \mathbf{J}_0^{-1}. \tag{38a}$$

where $j^{h,e}$, j_0 and $\mathbf{J}_0$ are given in (13b) and (18), respectively. The special structure with the element-wise constant quantities j_0 and $\mathbf{J}_0$ ensures that the patch test is fulfilled by construction of the enhanced field (see Section 2.4). Other possibilities, which

are compared to (38a) in Section 3.7 are

$$\mathbf{M}_I = \frac{j_0}{j^{h,e}} \mathbf{J}_0 \hat{\mathbf{M}}_I \mathbf{J}_0^{-1}, \tag{38b}$$

$$\mathbf{M}_I = \frac{j_0}{j^{h,e}} \mathbf{J}_0 \hat{\mathbf{M}}_I \mathbf{J}_0^{\mathrm{T}}, \tag{38c}$$

$$\mathbf{M}_I = \frac{j_0}{j^{h,e}} \mathbf{J}_0^{-\mathrm{T}} \hat{\mathbf{M}}_I \mathbf{J}_0^{\mathrm{T}}, \tag{38d}$$

$$\mathbf{M}_I = \frac{j_0}{j^{h,e}} \mathbf{J}_0^{-\mathrm{T}} \hat{\mathbf{M}}_I, \tag{38e}$$

$$\mathbf{M}_I = \frac{j_0}{j^{h,e}} \mathbf{J}_0^{\mathrm{T}} \hat{\mathbf{M}}_I, \tag{38f}$$

$$\mathbf{M}_I = \frac{j_0}{j^{h,e}} \hat{\mathbf{M}}_I \mathbf{J}_0^{-1}, \tag{38g}$$

$$\mathbf{M}_I = \frac{j_0}{j^{h,e}} \hat{\mathbf{M}}_I \mathbf{J}_0^{\mathrm{T}}, \tag{38h}$$

$$\mathbf{M}_I = \frac{j_0}{j^{h,e}} \hat{\mathbf{M}}_I. \tag{38i}$$

All of the options listed above can furthermore be used with an element-wise average jacobian in analogy to (36) given by

$$\mathbf{J}_{avg} = \frac{1}{V} \int_{\Omega_e} \mathbf{J}^{h,e} \, \mathrm{d}V \tag{39}$$

instead of the Jacobian $\mathbf{J}_0$ evaluated at the element center (18).

Remark 9. Note, that (38b) is used in [1] and (38c) is similar to a *push-forward* of a *contravariant* tensor (used e.g. by [28]), whereas (38a) resembles *push-forward* of a *covariant* tensor. However, so far (38a) seems to be working best (cf. [22,27] and Section 3.7). Refer to Appendix A for a motivation based on curvilinear coordinates of some of the transformations listed above.

The first set of shape functions $\mathbf{M}_I$ used in the present work for the enhanced field are the *Wilson-modes* presented by [8]. They assume the form

$$\sum_{I=1}^{9} \hat{\mathbf{M}}_I \alpha_I = \begin{bmatrix} \xi\alpha_1 & \eta\alpha_2 & \zeta\alpha_3 \\ \xi\alpha_4 & \eta\alpha_5 & \zeta\alpha_6 \\ \xi\alpha_7 & \eta\alpha_8 & \zeta\alpha_9 \end{bmatrix} \tag{40}$$

in the current framework. Unfortunately, these shape functions lead to severe *hour-glassing* in compression even if only simple hyperelastic materials are used (cf. Section 3.4 and [41,43,22,26,19]). Thus, Korelc and Wriggers [19] suggested using the transpose of (40) (see also [22,35,26]), as it removes *hour-glassing* at least in compression and for hyperelastic materials. This is proven analytically in e.g. [19,22,26].

Finally, the purely volumetric shape functions additionally introduced on top of the *Wilson-modes* by Simo et al. [1] are considered in the present work. They are given by

$$\sum_{I=10}^{12} \hat{\mathbf{M}}_I \alpha_I = \left(\eta\zeta\alpha_{10} + \xi\zeta\alpha_{11} + \xi\eta\alpha_{12} \right) \mathbf{I}, \tag{41}$$

where $\mathbf{I}$ denotes the unity tensor. Note that there are no additional modes analogous to (41) in the 2D case.

A very important requirement on the choice of shape functions for the enhancement is that the discrete ansatz-spaces for the deformation and the enhanced field may have no intersection. Namely, condition

$$\mathrm{Grad}[\mathcal{U}^h] \cap \mathcal{F}^h = \emptyset \tag{42}$$

has to hold for the discrete ansatz spaces $\mathcal{U}^h$ and $\mathcal{F}^h$ given in (11) and (32), respectively. This condition ensures stability of the method in linear analysis (cf. [3,39]) and is crucial in nonlinear simulations as well. However, other factors can still lead to instabilities in the nonlinear regime (cf. [41,43,22,19,26,35,2] among others).

Remark 10. Note that (40) can alternatively be written as dyadic product of the form

$$\sum_{I=1}^{9} \hat{\mathbf{M}}_I \alpha_I = \sum_{J=1}^{3} \boldsymbol{\beta}_J \otimes \hat{\mathbf{G}}_J(\boldsymbol{\xi}), \tag{43}$$

where $\boldsymbol{\beta}_1 = \begin{bmatrix} \alpha_1 & \alpha_4 & \alpha_7 \end{bmatrix}$ and $\hat{\mathbf{G}}_1 = \begin{bmatrix} \xi & 0 & 0 \end{bmatrix}$. The other $\boldsymbol{\beta}_J$ and shape functions $\hat{\mathbf{G}}_J$ for $J = 2, 3$ are defined accordingly. Since (43) has the same structure as (14) (without transformations), $\boldsymbol{\beta}_J$ are referred to as incompatible displacements. Other types of shape functions cannot be put into this framework that simple, since they cannot be written in the same dyadic form. There is however always a possibility with more complex notation as shown by Bischoff and Romero[10].

If the shape functions for enhancement can be given in the simple form (43) it is possible to greatly simplify the discrete equations emerging from (8). Inserting (43) together with (38a) and (34) into (32) yields

$$\tilde{\mathbf{F}}^{h,e} = \sum_{J=1}^{3} \frac{j_0}{j^{h,e}} \mathbf{F}_0 \mathbf{J}_0^{-T} \left(\boldsymbol{\beta}_J \otimes \hat{\mathbf{G}}_J \right) \mathbf{J}_0^{-1}. \tag{44}$$

Defining $\boldsymbol{\gamma}_J = \mathbf{F}_0 \mathbf{J}_0^{-T} \boldsymbol{\beta}_J$ as new degrees of freedom finally recasts the last equation into the form

$$\tilde{\mathbf{F}}^{h,e} = \sum_{J=1}^{3} \frac{j_0}{j^{h,e}} \boldsymbol{\gamma}_J \otimes \left(\mathbf{J}_0^{-T} \hat{\mathbf{G}}_J \right) \tag{45}$$

which does not depend on $\boldsymbol{\varphi}$ and has, apart from the multiplication with the determinants j_0 and $j^{h,e}$, the exact same structure as (14) (cf.[1]). This makes numerical implementation of elements employing shape functions of the form (43) especially easy, since variations and linearisations with respect to $\boldsymbol{\varphi}$ vanish. Note, that this scheme does not depend on (38a) and (34) but works with all other transformations listed in (38) and (32).

2.2.3 | Stresses

The remaining field to be discretized for a full discrete form of (8) are the stresses $\mathbf{P}$ defined in (5). Its approximation is done analogously to (32) and given by

$$\mathbf{P}^h \in \mathcal{P}^h = \left\{ \mathbf{P}^h \in \mathcal{P} \, \middle| \, \mathbf{P}^h = \sum_{e=1}^{n_{el}} \chi_e \mathbf{P}^{h,e}(\mathbf{X}) \right\}, \tag{46}$$

with the frame invariant interpolation functions $\mathbf{P}^{h,e}$, which have to include at least constant stresses in order to fulfil the patch test (see Section 2.4 and Simo and Rifai[3]). The exact form of $\mathbf{P}^{h,e}$ is not needed, as the stresses are eliminated via an orthogonality condition (refer to Section 2.3).

2.3 | Orthogonality Condition

The stress field $\mathbf{P}^h$ is eliminated from the discrete version of (8) by setting $\mathcal{P}^h$ L_2-orthogonal to $\tilde{\mathcal{F}}^h$. Thus, the equation system (8) can be reduced to

$$\delta_{\boldsymbol{\varphi}} \Pi_{\text{mix}}^h = \int_{\mathcal{B}_0^h} \hat{\mathbf{P}}^h : \delta_{\boldsymbol{\varphi}} \mathbf{F}^h \, dV + \Pi_{\text{ext}}^h (\delta \boldsymbol{\varphi}^h) = 0, \tag{47a}$$

$$\delta_{\boldsymbol{\alpha}} \Pi_{\text{mix}}^h = \int_{\mathcal{B}_0^h} \hat{\mathbf{P}}^h : \delta_{\boldsymbol{\alpha}} \mathbf{F}^h \, dV = 0, \tag{47b}$$

in a discrete setting, which is the basis for a finite element implementation. The relations covering orthogonality and elimination of the discrete stresses presented here are based on the works of Simo et al.[3,4].

2.4 | Patch test condition

An important requirement for any finite element is that it fulfills the *patch test*, meaning that the response of an elastic solid subject to a constant state of strain is exactly reproduced for arbitrarily distorted patches of elements (see[54,55]). For the classical EAS method this puts some restrictions on the shape functions $\hat{\mathbf{M}}_I$ introduced in (38) (cf. e.g.[3,4,26]). Note, that the following

statements are only valid if the compatible deformation gradient presented in Section 2.2.1 fulfills the patch test. Thus the compatible deformation gradient must be computed either in the standard way using (15) or with the modified version of approach (28) by Simo et al.. The patch test is violated in distorted meshes, if the gradient of shape functions (16) presented by Simo et al.[1] is used. Refer to Appendix C for more information on the patch test and the compatible field as well as an analytic proof, that the novel approach fulfills the patch test.

Two important conclusions can be drawn from the imposed constant strains $\mathbf{F}^{h,e} = \mathbf{F}_0$. Firstly, they imply constant constitutive stresses $\hat{\mathbf{P}} = \mathbf{P}_0 = $ const. for homogeneous materials, which are assumed in the present work. Secondly,

$$\tilde{\mathbf{F}}^{h,e} = \bar{\mathbf{F}}^e = \mathbf{0} \qquad \Rightarrow \qquad \mathbf{F}^{h,e} = \mathbf{F}_\varphi^{h,e} = \mathrm{D}\boldsymbol{\varphi}^{h,e} = \mathbf{F}_0 \tag{48}$$

follows from condition (42) and the fact that the space of compatible deformation $\mathcal{U}^h$ (11) includes constant strains[5]. Note that $\delta\tilde{\mathbf{F}}^{h,e} \neq \mathbf{0}$ as the variations are arbitrary.

Ultimately, (47) has to be fulfilled exactly by the approximated fields to satisfy the patch test. Imposing conditions $\hat{\mathbf{P}} = \mathbf{P}_0 = $ const. and (48) on (47a) yields

$$\int_{\mathcal{B}_0^h} \mathbf{P}_0 : \mathrm{D}\delta\boldsymbol{\varphi}^h \ \mathrm{d}V + \Pi_{\text{ext}}^h(\delta\boldsymbol{\varphi}^h) = 0 \tag{49}$$

for all admissible variations $\delta\boldsymbol{\varphi}^h$. This equation is fulfilled as it is equivalent to a pure displacement formulation, which satisfies the patch test if the approximation is chosen appropriately. Inserting the same relations into (47b) yields

$$\sum_{e=1}^{n_{el}} \mathbf{P}_0 : \int_{\Omega_e} \delta_{\boldsymbol{\alpha}}\mathbf{F}^{h,e} \ \mathrm{d}V = 0. \tag{50}$$

With definitions (32), (37), (38) and by transforming the integral to the reference element we finally arrive at

$$\int_{\hat{\Omega}} \hat{\mathbf{M}}_I \ \mathrm{d}\hat{\Omega} = \mathbf{0} \tag{51}$$

which has to hold for all shape functions $\hat{\mathbf{M}}_I$ for the enhanced part of the deformation gradient. It is straightforward to show that this condition is fulfilled by shape functions (40) and (41). Note, that the form of (38) with the determinant of the Jacobian matrix (13b) in the denominator enables the simple form of (51).

3 | NUMERICAL INVESTIGATIONS

This section covers standard numerical tests to evaluate the performance of the different transformations and shape functions presented in Section 2. Among the properties of interest are objectivity, sensitivity to mesh distortion, convergence behavior, stability of the elements and the patch test requirement. Furthermore, shear and volumetric locking are examined. All elements tested are based on 8-node brick elements in 3D and 4-node quadrilateral plain strain elements in 2D and use the standard 8- and 4-point quadrature rule if not stated otherwise. The elements are identified as follows:

- **H1:** Three-dimensional isoparametric displacement formulation using the standard gradient of shape functions (15). The corresponding 2D element is denoted Q1.

- **HM1:** Isoparametric displacement formulation using the modified gradient of shape functions (16) introduced by Simo et al.[1].

- **H1/E9:** EAS element introduced by Simo and Armero[4] employing the Wilson-modes (40) for the enhanced field. Thus, there are nine additional enhanced parameters. The corresponding 2D element is denoted Q1/E4 and has 4 additional modes. If not stated otherwise, H1/E9 uses transformations (38a) and (34), which can be simplified for the given element (see Remark 10). Other transformations listed in (38) are denoted by suffixes of the form $J_0(x)$, where "x" is a letter from "a" to "i" corresponding to the transformations given in (38a) to (38i). Furthermore, J_0 is replaced by J_{avg} if the average jacobian (39) is used instead of the evaluation at the element centroid (18).

---

[5] Since the isoparametric displacement element fulfills the patch test. This holds as well for modification (28) but not for (16).

- **H1/E9T**: EAS element using the transpose of the Wilson-modes as introduced by Glaser and Armero[22][6]. The standard transformations used for this element are again (38a) and (34). Alternatives for transformation matrix $\mathbf{T}_0$ introduced in (32) are denoted by suffixes F_0^{-T} if the newly proposed option (35) is used and by "nonObj" for the non-objective choice $\mathbf{T}_0 = \mathbf{I}$. Other transformations regarding the shape functions of the enhanced modes, which are listed in (38), are denoted as described for element H1/E9.

- **HM1/E12:** Element with twelve enhanced modes as presented by Simo et al.[1]. It uses the Wilson-modes (40) and 3 additional modes (41) as well as the modified gradient (16) and a special 9-point quadrature rule (see e.g.[1,35]). The only difference of the corresponding 2D element QM1/E4 to Q1/E4 is the quadrature rule.

- **HM1/E12T:** Analogous to HM1/E12 but employing the transpose of the Wilson-modes (40) in addition to (41) as shape functions for the enhanced deformation gradient.

- **H1/E12** and **H1/E12T:** Equivalent to HM1/E12 and HM1/E12T but using the standard gradient (15) of the shape functions for the conforming part of the deformation gradient instead of the modified version (16). Suffix F_0^{-T} is added if the novel transformation (35) is applied for frame invariance of the enhanced modes.

- **HA1/E12** and **HA1/E12T:** Equivalent to HM1/E12 and HM1/E12T but using the improved version of the gradient of the shape functions given in (28), which fulfills the patch test in contrast to (16). Again, we use suffix F_0^T to denote application of the novel transformation (35).

The material model used for all simulations in this work is a *Mooney-Rivlin-model* with strain energy function

$$W(\mathbf{C}) = a \left(I_1(\mathbf{C}) - 3\right) + b \left(I_2(\mathbf{C}) - 3\right) + \frac{c}{2} \left(\sqrt{I_3(\mathbf{C})} - 1\right)^2 - d \log\left(\sqrt{I_3(\mathbf{C})}\right), \tag{52}$$

where $I_1(\mathbf{C})$, $I_2(\mathbf{C})$ and $I_3(\mathbf{C})$ denote the invariants of the right *Cauchy-Green-tensor* $\mathbf{C} = \mathbf{F}^T\mathbf{F}$. The scalars a, b, c, with $a, b, c > 0$ for polyconvexity[56], are the three independent material parameters of the model and $d = 2a + 4b$ depends on the other parameters.

3.1 | Patch test

The first test to assess the elements presented above is the standard patch test (see[57,55]), where a deformation state is applied such that constant strains occur. The required outcome is constant stress for homogeneous materials (see section 2.4). It is an important condition, that any finite element has to fulfill (cf.[55]). For the EAS elements presented in the previous Section 2, it is shown in Section 2.4, that the patch test is fulfilled by design if condition (51) holds (which is the case for all shape functions considered here) and the compatible deformation gradient fulfills the patch test. This is the case if the standard gradient of shape functions (15) or modification (28) is used (see[47,51]). However, employing (16) leads to a violation of the patch test. Corresponding analytic investigations are presented in Section 2.4 and Appendix C. The numerical examples below are included to verify those results.

The test is performed on a unit cube $\mathcal{B}_0 = [0, 1] \times [0, 1] \times [0, 1]$ in 3D and a unit square $\mathcal{B}_0 = [0, 1] \times [0, 1]$ in 2D, respectively. Dirichlet boundary conditions

$$u_i(X_i = 0, X_j, X_k) = 0 \tag{53}$$

are applied on the lower surfaces ($X_i = 0$), implying that there is no deformation in the respective directions and yielding restraint free bearings. Constant strains are introduced by imposing an additional boundary condition

$$u_3(X_1, X_2, X_3 = 1) = u \tag{54}$$

on the upper surface $X_3 = 1$ (analogously in 2D with u_2 and $X_2 = 1$). Displacement u is increased in steps of $\Delta u = 0.05$ until the *Newton-Raphson* scheme finds no solution. The material parameters for chosen Mooney-Rivlin material (52) are set to

$$a = 1.538 \cdot 10^5, \qquad b = 7.692 \cdot 10^4, \qquad c = 2.692 \cdot 10^5, \tag{55}$$

---

[6]The transpose Wilson-modes were first suggested by Korelc and Wriggers[19] but the element presented there lacks frame invariance as shown in Glaser and Armero[22]. In the present framework, the non-objective element presented by Korelc and Wriggers[19] is denoted by H1/E9T-nonObj in 3D and Q1/E4T-nonObj in 2D.
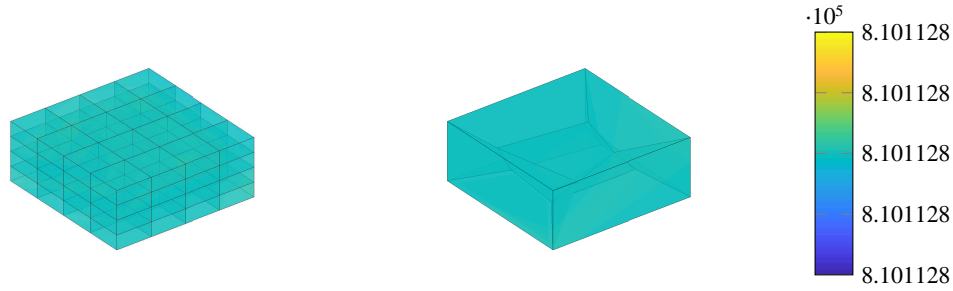
FIGURE 2 Three-dimensional regular (left) and distorted (right) patch test. Deformed configuration at $u = 0.55$ with von Mises stress distribution. Figures generated with H1 element.

which correspond to $E = 10^6$ and $v = 0.3$ in linear theory. This leaves only the FE-mesh to complete the configuration of the patch test. A regular 3D mesh with $4 \times 4 \times 4$ elements is chosen in addition to an initially distorted[7] mesh (see Fig. 2). The 2D meshes are chosen accordingly.

As expected, all 2D elements and 3D elements using the standard isoparametric approach with standard gradient of the shape functions (15) or the improved version of the approach by Simo et al. (28) pass the patch test. This is in line with the investigations shown in Section 2.4, Remark 6 and Appendix C. Unfortunately, 3D elements using the modified gradient (16) (HM1, HM1/E12 and HM1/E12T) only pass the patch test in case of the regular mesh, a fact first noted by Wriggers and Korelc[21] (see also Müller-Hoeppe et al.[34] and Areias et al.[45]).

The fulfillment of the patch test can be quantified by looking at the mean value and standard deviation of the *von Mises* stresses of the modeled body. A typical element fulfilling the requirements shows for a displacement of $u = 0.4$ a mean value of $\sigma_{\text{mean}} = 4.978e5$ (exact value) and a small standard deviation of approx. $\sigma_{\text{dev}} \approx 1e-9$[8] for any mesh. An element violating the patch test, such as e.g. HM1, exhibits a slightly different mean value $\sigma_{\text{mean}} = 4.965e5$ and a high standard deviation $\sigma_{\text{dev}} \approx 1e4$ quantifying the violation of the test.

3.2 | Objectivity

The goal of this test is to show that the elements are objective, meaning that their response is invariant to rigid body motions. The test is taken from[22] (see also e.g.[35]) and its geometry is depicted in Figure 3.

The beam-like structure has a length of $L = 1.0$ and its other dimensions are $h = b = 0.1$. Dirichlet boundaries are imposed on both ends of the beam with prescribed displacements

$$\mathbf{u}_1 = \mathbf{Q}(\theta_i)\mathbf{X}, \qquad \mathbf{u}_2 = \mathbf{Q}(\theta_i)\left(\mathbf{X} + u_i\mathbf{e}_y\right), \qquad i = 1, \dots, n \tag{56}$$

assigned to the left and right end of the undeformed beam $\mathcal{B}_0$, respectively. They are applied during n steps in which the scalar displacement $u_i = u \cdot i/n$ is increased to the final magnitude $u = 2h$. Furthermore, rigid body motions are imposed on the beam through rotation matrix

$$\mathbf{Q}(\theta_i) = \begin{bmatrix} \cos(\theta_i) & -\sin(\theta_i) & 0 \\ \sin(\theta_i) & \cos(\theta_i) & 0 \\ 0 & 0 & 1 \end{bmatrix} \in \text{SO(3)}, \qquad \theta_i = \theta \cdot i/n \tag{57}$$

where the final angles of rotation are chosen as $\theta \in \{0, 15, 30, 45, 60, 75, 90\}°$ (cf.[22]). The number of load steps is $n = \theta/3 + 1$ for any given final angle θ. All final configurations of the continuum are shown in Figure 3 and were computed using a mesh with only six elements. Furthermore, the Mooney-Rivlin material (52) is used with parameters $a = 40$, $b = c = 10$, which correspond to $\lambda = 50$ and $\mu = 100$ or equivalently $E = 233.3$, $v = 0.1667$ in linear theory.

Frame invariance is finally verified by examining the reaction forces at the bearings. This is done in a beam like manner by summarizing the nodal forces in the rotated local coordinate system into axial force N, shear force V and bending moment M.

---

[7]The geometry of the distorted mesh is chosen according to[57].
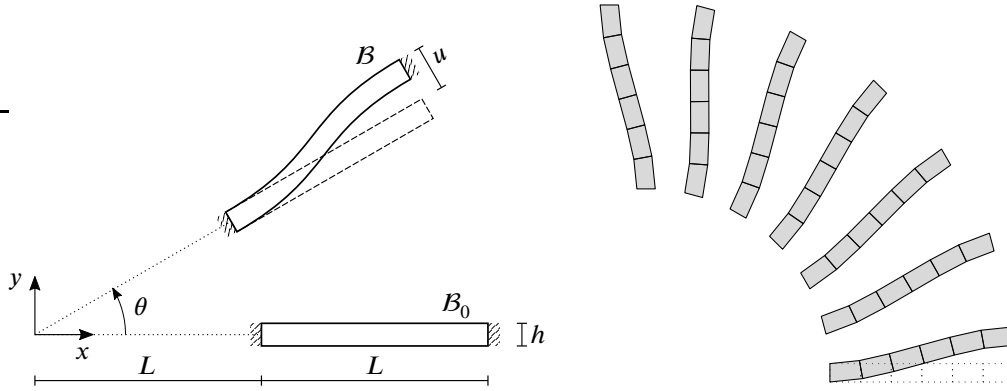
[8]Due to round-off errors.

FIGURE 3 Geometry of the objectivity test (left) and all final configurations (right). Reference configuration depicted with dotted lines. Plot on right side generated with 2D element Q1/E4.
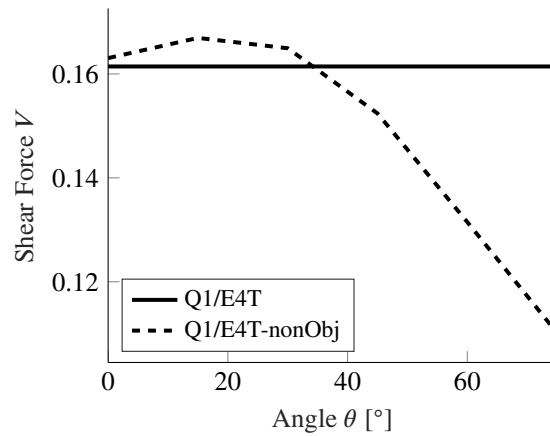

FIGURE 4 Demonstration of violation of objectivity by element Q1/E4T-nonObj. Shear force V at right bearing for different angles θ (see also [22]).

There may be no change in these values for an element to be objective, which is quantified by the standard deviation, of the reaction forces for different angles θ. All elements with the exception Q1/E4T-nonObj pass this test with standard deviations of the forces being below $1 \cdot 10^{-8}$. The clearly non-objective response of Q1/E4T-nonObj is depicted in Fig. 4 and compared to the correct behavior of Q1/E4T. We stress that the newly proposed formula (35) for the transformation of the enhanced deformation gradient does pass the present objectivity test.

3.3 | Linearized Eigenvalue analysis

The next test is the linearized eigenvalue analysis first presented for EAS elements by Simo et al. [1] (see also [13,28,24,58]). It is used to determine the locking behavior of elements in the incompressible limit, which is approximately enforced by setting

$$a = 0.35, \qquad b = 0.15, \qquad c = 1 \cdot 10^9 \tag{58}$$

for the Mooney-Rivilin material (52). This corresponds to a ratio $K/\mu = 1 \cdot 10^9$ for the bulk modulus K and shear modulus μ in linear theory. A single element, either distorted or regular (see Fig. 5), is considered for this test and a spectral eigenvalue analysis is then conducted on its tangent matrix in the stress free reference configuration. This yields 24 modes for the 3D-elements and 8 modes for the 2D versions, which is equal to the respective number of displacements DOFs. Additional modes for the enhanced DOFs do not occur because static condensation (cf. e.g. [3,4]) eliminates these DOFs on element level.

The computed eigenvalues λ_i are summarized in three groups: rigid body modes with $\lambda_i = 0$, soft modes with finite λ_i and locking modes with $\lambda_i \to \infty$[9]. A completely locking free element should exhibit only one eigenvalue tending to infinity. The corresponding mode represents pure volumetric deformations (see [1,28]). Furthermore, there have to be six rigid body modes with $\lambda_i = 0$ in 3D and only three in 2D, representing the number of possible independent motions of a rigid body. The right number of rigid body modes is recovered by all presented elements (see Tab. 1 and 2). All remaining modes should have finite eigenvalues and represent the deformation behavior of the elements.
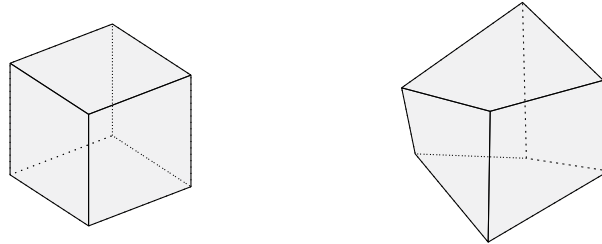

FIGURE 5 Regular (left) and distorted (right) element in 3D.

However, these ideal results are not obtained in the numeric analysis as most elements fail to reproduce the desired outcome with only one locking mode. The number of modes in each category is shown in Tables 1 and 2 for some examined 3D elements. Note, that the seven locking modes of H1 and HM1 for the regular cube show their severe locking, which gets even worse in distorted meshes for element H1 with an additional "high" mode. Enhancement with Wilson-modes (H1/E9) or the transpose thereof (H1/E9T, H1/E9T-F_0^{-T}), which give identical results in this test[10], reduces locking but cannot completely eliminate it. This behavior is sometimes referred to as *mild locking* (see [1]) and has drawbacks especially if elasto-plastic materials are used (cf. Andelfinger et al. [38]). Using different transformations for the enhanced field listed in Section 2.2.2 does not change the number of locking modes in each category but slightly changes their values which renders more and less effective transformations. This is further elaborated upon in the Cooks-membrane test in Section 3.7.

The only elements exhibiting the desired behavior with only one locking mode in both the regular and distorted mesh are the elements using one of the modified versions of the gradient of shape functions (16) or (28) in addition to 12 enhanced modes (HM1/E12(T), HA1/E12(T) and HA1/E12T−F_0^{-T}). However, element HM1/E12 as well as HM1/E12T, which use gradient (16), violate the patch test (see Section 2.4 and 3.1). If the modification of the compatible deformation gradient is omitted (e.g. H1/E12 and H1/E12T-F_0^{-T}), the element fulfills the patch test but shows two extra locking modes for the distorted cube. Only the novel approach based on (28) is able to maintain both - *completely* locking-free behavior for arbitrary meshes and fulfillment of the patch test.

In the 2D plain-strain case, the only elements subject to locking are Q1 and QM1. All other elements exhibit only one mode tending towards infinity and are thus completely locking free.

3.4 | Stability analysis

The next test is the stability analysis introduced by Reese[42] to examine if elements are prone to hour-glassing. This phenomenon has first been thoroughly covered for EAS elements by[42,41] and is a major drawback of the original geometrically non-linear EAS element based on Wilson-modes presented by[4]. More recent results by Sussman and Bathe[37] show, that hour-glassing is even possible for small strains if the geometric aspect ratio of the elements is large. This makes an hour-glassing free element even more important. Note, that the stability test is often conducted in an analytic setting (see e.g. [42,41,26,22,2,37,35]) in contrast to the numerical investigation presented in[43] and the present work. However, the same conclusions can be drawn.

The stability analysis is performed on a single element (see Fig. 6) with exactly the same dimensions as the reference element presented in Section 2.2.1, making the transformations especially simple. The material parameters of model (52) are chosen to

---

[9]Infinity is not reproduced in the numeric analysis as incompressibility is only approximated by a high ratio of K/μ. This means that in this benchmark modes with "high" eigenvalues are considered as locking modes.

[10]Since the linearization of H1/E9 and H1/E9T yield the same linear element. In fact, both coincide with the original EAS element proposed by Simo and Rifai[3].

TABLE 1 Results of spectral eigenvalue analysis of initial stiffness matrix, regular cube - selected elements

Element Type	number of modes - regular		
	rigid body[1]	soft modes[2]	locking modes[3]
H1	6	11	7
HM1	6	11	7
H1/E9	6	14	4
H1/E9T	6	14	4
H1/E9T-F_0^{-T}	6	14	4
H1/E12	6	17	1
HM1/E12	6	17	1
HA1/E12	6	17	1
HA1/E12T-F_0^{-T}	6	17	1

[1] number of spectral eigenvalues $|\lambda_i| \leq 1 \cdot 10^{-4}$
[2] number of spectral eigenvalues $1 \cdot 10^{-4} \leq \lambda_i \leq 1 \cdot 10^2$
[3] number of spectral eigenvalues $\lambda_i \geq 1 \cdot 10^2$ ("$\lambda_i \to \infty$")

TABLE 2 Results of spectral eigenvalue analysis of initial stiffness matrix, distorted cube - selected elements

Element Type	number of modes - distorted		
	rigid body[1]	soft modes[2]	locking modes[3]
H1	6	10	8
HM1	6	11	7
H1/E9	6	13	5
H1/E9T	6	13	5
H1/E9T-F_0^{-T}	6	13	5
H1/E12	6	15	3
HM1/E12	6	17	1
HA1/E12	6	17	1
HA1/E12T-F_0^{-T}	6	17	1

[1] number of spectral eigenvalues $|\lambda_i| \leq 1 \cdot 10^{-4}$
[2] number of spectral eigenvalues $1 \cdot 10^{-4} \leq \lambda_i \leq 1 \cdot 10^2$
[3] number of spectral eigenvalues $\lambda_i \geq 1 \cdot 10^2$ ("$\lambda_i \to \infty$")

$a = 9$, $b = 1$ and $c = 99996$ representing a nearly incompressible material with $\mu = 20$ and $\lambda = 10^5$ (corresponding to a Poisson ratio of $\nu = 0.4999$ in the linear case). Dirichlet boundaries are applied analogously to the patch test shown in Section 3.1, to gain a restraint free setting. The structure is loaded by imposing prescribed deformations on the top face ($y = 1$) and thereby determining the stretch λ_2. Despite being non-linear, an analytic solution for λ_1 can be found for the problem at hand. Thus, all displacements are determined and the exact deformation state can be imposed on the given element. Finally solving the eigenvalue problem

$$\mathbf{K}_{red}\mathbf{x}_i = \omega_i \mathbf{x}_i, \tag{59}$$

of the reduced tangential stiffness matrix $\mathbf{K}_{red}$ (excluding DOFs with imposed Dirichlet boundary conditions) for a given configuration yields the eigenvalues ω_i and corresponding eigenvectors $\mathbf{x}_i$. Instability points (singular points) are characterized by a zero eigenvalue. Furthermore, negative eigenvalues imply that the equilibrium is unstable (see[2]). Note, that there are also physical singular points for the given problem (see Glaser and Armero[22]) but they do not occur if the specimen is modeled with a single element (cf.[37] and Section 3.5).

All in all, the eigenvalues of $\mathbf{K}_{red}$ must fulfill $\omega_i > 0$, which implies that only the lowest eigenvalue ω_1 has to be examined to determine if any instabilities occur. The value of ω_1 is plotted against stretch λ_2 in Figure 7 [11] for some tested EAS elements.

---

[11] Note, that states of compression are characterized by $\lambda_2 < 1$.
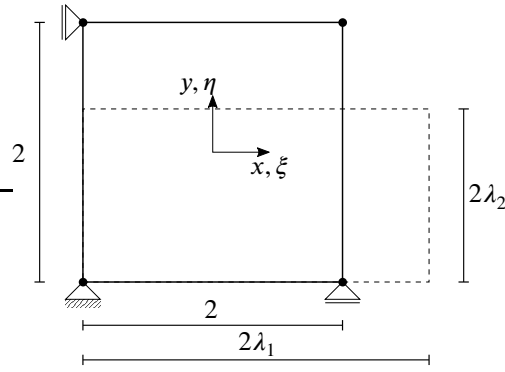
FIGURE 6 Geometry and constraints for the 2D stability test (extended in the present work for hexaedral elements). Deformed configuration depicted with dashed line.
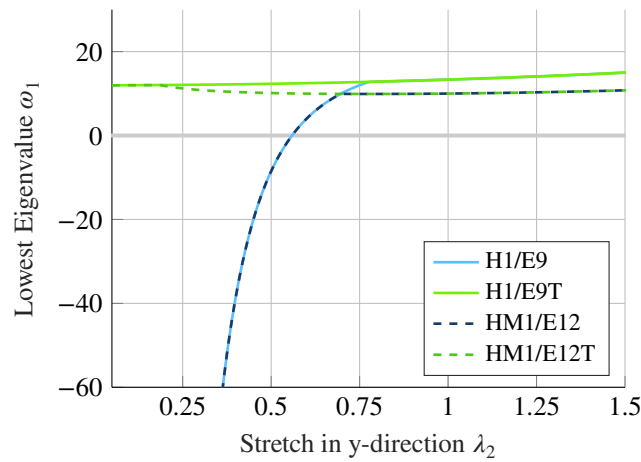

FIGURE 7 Stability test results: selected 3D elements. Lowest eigenvalue ω_1 plotted against stretch λ_2.

Evaluating these plots shows that only elements employing the Wilson-modes for the enhanced field (40) exhibit negative eigenvalues. This is true whether the additional modes (41) are used or not. These instabilities occur under compression at $\lambda_2 \approx 0.61$ for the given geometry and material. Unfortunately, Sussman and Bathe[37] have shown that for elements with high aspect ratios instabilities already occur for small deformations with $\lambda_2 = 0.99$, which renders elements exhibiting negative eigenvalues almost unusable. Elements using the transpose of the Wilson-modes (H1/E9T, HM1/E12T) exhibit no negative eigenvalues and are therefore at least for the considered polyconvex hyperelastic materials stable. However, hourglassing still occurs for other kinds of materials, e.g. the frequently used elasto-plastic material by Simo[59]. This has for instance been reported by Armero[26] for element Q1/E4T, which is unconditionally stable for elastic materials without material instabilities. The consideration of a elasto-plastic material model is however beyond the scope of the present work.

Note, that the type of transformation of the enhanced field and compatible field (see Sections 2.2.1 and 2.2.2) has no impact on the results listed above.

3.5 | Large mesh stability test

This test is included to verify the results form the one-element stability analysis presented in Section 3.4 above with larger FE-meshes. This shows the elements' hour-glassing behavior in combination with neighboring elements and also the ability to depict physical instabilities. The test presented here is mainly taken from the works of Glaser and Amero[22] and Korelc et al.[35]. It is performed with the same material properties as the stability test in Section 3.4 on a cube (see Fig. 8) with an edge length of $a = 50$, which is discretized with 12 elements per side in a regular manner (see Fig. 8).
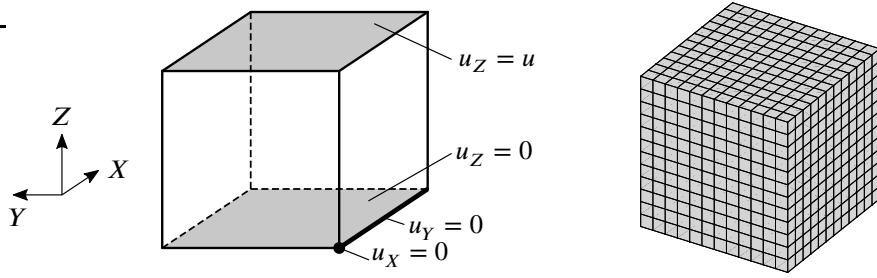
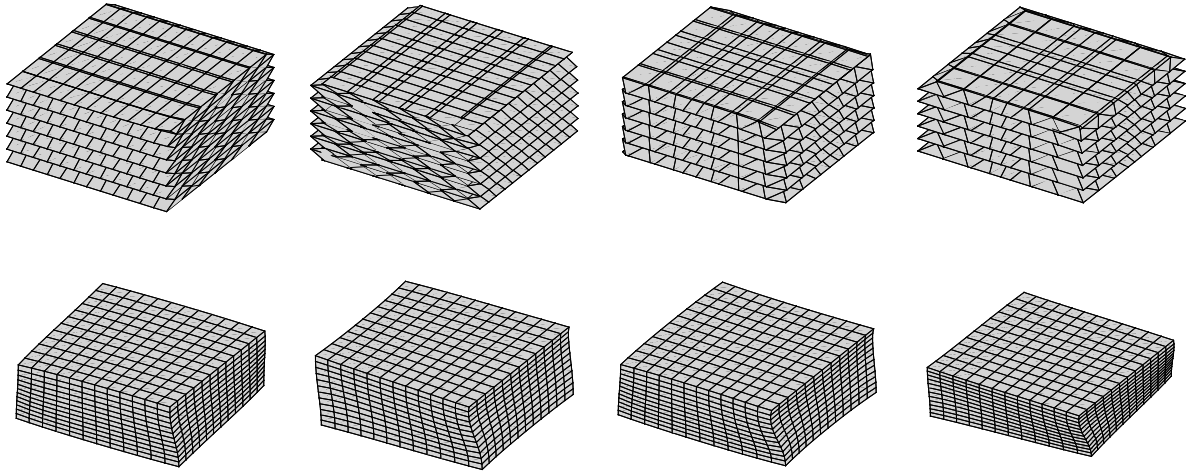**FIGURE 8** Large mesh stability test. Geometry and mesh.

FIGURE 9 First four eigenmodes of H1/E9 (top) and H1/E9-T

Dirichlet boundary conditions $u_X = u_Y = u_Z = 0$ are applied on the corner node, one edge and lower surface as shown in Figure 8. The cube is loaded analogously to the one-element stability test by prescribed displacements $u_Z = u_i$ on the top surface. Again, a analytic (homogeneous) solution to the problem at hand can easily be found with a principal stretch based version of (52). This solution is imposed on the system by assigning these analytically obtained displacements to the nodes. Finally, an eigenvalue analysis (59) is performed on the stiffness matrix at that deformed state. Eigenvalues $\omega_i = 0$ characterize instability points which are determined approximately by gradually increasing the prescribed displacement u_i in steps of $\Delta u_i = 0.01a$. The procedure is repeated until either four stability points are passed or a displacement $u_i = 0.8a$ is reached. Determining and plotting the corresponding eigenvectors at states with $\omega_i \approx 0$ enables to decide if the instability is physical or unphysical (hour-glassing).

Four instability points are detected for all elements considered with the exception of the purely displacement based elements, which are not able to reproduce that behavior. As suggested by the previous test in Section 3.4 the remaining elements can be classified into two main groups. The first one contains all elements based on Wilson modes and show severe hour-glassing. The second one contains the ones based on transpose Wilson modes where only physical modes appear. Figure 9 shows the eigenmodes corresponding to the first four negative eigenvalues of H1/E9 and H1/E9T which are representative for their respective groups. All four nonphysical eigenvectors of H1/E9 depicted in Fig. 9 occur at a state of compression of $\lambda_1 \approx 0.61$ ($u = 0.39$) which is in line with the results given in Section 3.4, where the instability was detected at exactly the same level. Physical instabilities of element H1/E9T first arise as the block is compressed to 55% of the initial height ($\lambda_1 \approx 55\%$). Using the additional enhanced modes (41) has only minor effects on the compression state at which the first instability occurs and does not change the shape of the computed eigenvectors. Note, that higher eigenmodes are affected more (e.g. the fourth instability occurs at $\lambda_1 = 0.42$ for H1/E9T and at $\lambda_1 = 0.51$ for HA1/E12TF_0^{-T}) but still the mode shape remains roughly the same. Furthermore, neither the type of transformations for the compatible deformation gradient in Section 2.2.1, nor the transformations listed in (38) have any effect on the results.
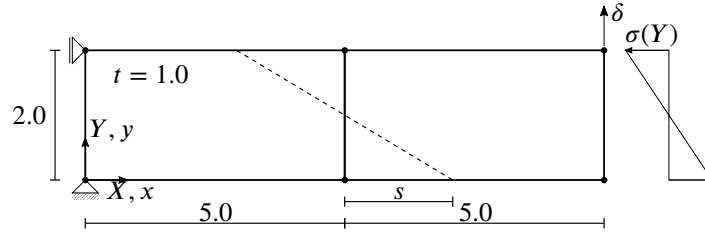
FIGURE 10 Geometry and boundary conditions for the mesh distortion test.
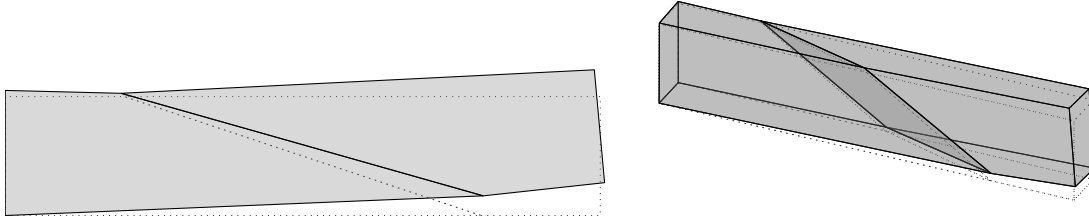

FIGURE 11 Deformed and undeformed configuration for $s = 3.0$ in 2D (left) 3D (right). Plots generated with standard EAS elements Q1/E4 and H1/E9.

3.6 | Mesh distortion

The next benchmark determines the element's behavior in distorted meshes. It is a standard benchmark e.g. included in [60,13,3,35,45,58] and usually performed on a cantilever-like structure, whose geometry and boundary conditions are shown in Figure 10. It is meshed with only two elements and mesh distortion is applied by moving the center nodes by s as indicated in Figure 10. Deformed and undeformed meshes for both the 2D and 3D case are shown in Figure 11. Note, that the nodes are moved unsymmetrically in the 3D case to get even more severely distorted elements. This is not the standard procedure but is applied here to get more insight into the distortion sensitivity of the elements. The material parameters of the Mooney-Rivlin model (52) are set to

$$a = 180, \qquad b = 120, \qquad c = 120, \tag{60}$$

which corresponds to the linear parameters $E = 1500$ and $\nu = 0.25$.

The test's setup is finished by applying a bending moment $M = 20$, assumed to be a dead load, on the right edge/face (see Fig. 10). This results under the assumption of simple beam theory in a linear distribution of stresses

$$\sigma(Y) = -30 \cdot (Y - 1), \tag{61}$$

which is only dependent on material coordinates Y and based on the reference area (dead load). All in all, this yields nodal forces with a magnitude of $F = \pm M/h = \pm 10$ if there are only two nodes on the right edge as shown in Figure 10.

The resulting normalized top edge displacements δ are presented in Figure 12, where they are plotted against the degree of skew s. Normalization of the displacements δ is conducted by comparing the computed deformations to the displacement δ_{ref} obtained from a simulation with a regular fine mesh with $40 \times 8 \times 4$ H1/E9 elements.

The plots in Figure 12a show selected 2D elements. The first conclusion that can be drawn from this plot is that the displacement element Q1 exhibits severe locking. All other elements give almost the exact result for $s = 0$ with deviations from the converged result below 1%. There is a small difference between Q1/E4, Q1/E4T and QA1/E4T, QA1/E4T-F_0^{-T} which is due to the additional Gauß-point of the latter elements. This coincides with the standard result for distorted isoparametric elements that the minimum number of Gauß-points yields the best results (cf. Zienkiewicz et al.[55] Chapter 5.12). In the present 2D case 4 points would suffice but note that the case is different in 3D where the additional Gauß-point is needed to integrate the volumetric enhanced modes (41) (see [1]). Furthermore, it can be observed that the various approximations of the compatible deformation gradient (Sec. 2.2.1) and the novel transformation using $\mathbf{F}_0^{-T}$ (35) have only very little effect on the present results.

In the 3D case (Fig. 12b), we observe again severe locking of the displacement formulation. Moreover, the effect of the distortion
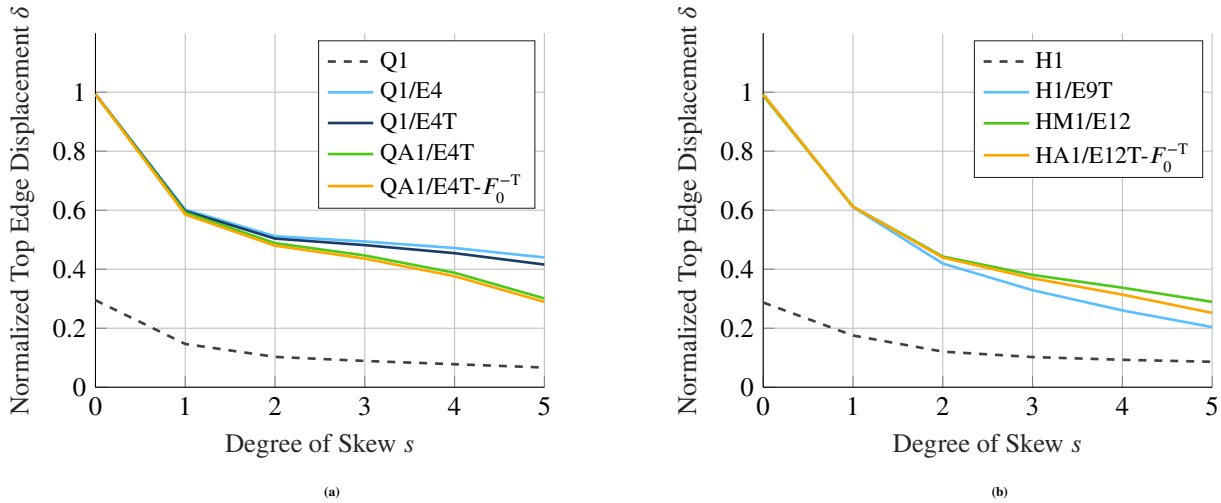
FIGURE 12 Mesh distortion test: normalized top edge displacement of selected 2D and 3D elements for different degrees of skew s

s is higher which is not surprising since the elements are more severely distorted due to the unsymmetric shift of nodes (see Fig. 11). The elements with nine enhanced modes (e.g. H1/E9T) perform worse than elements with twelve modes in this case showing the advantage of the additional modes (41). The overall best element HM1/E12 is only slightly better than the element HA1/E12T-F_0^{-T} which in contrast to HM1/E12 fulfills the patch test and is stable for hyperelastic materials (see Sections 2.4, 3.1 and 3.4).

Finally, the effect of the transformations (38) could be examined. However, these results are qualitatively identical to the outcome of the Cooks membrane test in Section 3.7, which is why they are omitted here.

3.7 | Cooks membrane

The final numerical test is the well-known Cooks membrane test (see e.g. [3,61,62,26,4,22,63,28,27,9]). It is designed to examine coarse mesh accuracy, convergence behaviour and shear locking in distorted meshes. Here, it is used to compare the performance of the various transformations and shape functions for the enhanced field presented in Section 2.2.

The general quadrilateral form and the clamped boundary condition on the left side of the Cooks membrane are depicted in Fig. 13. Shear stress $\tau = 100$ is applied on the right edge, which is high enough to yield large deformations (see Fig. 14). The parameters for Mooney-Rivlin material (52) are given by

$$a = 126, \qquad b = 252, \qquad c = 81661 \tag{62}$$

corresponding to $E = 2261$ and $\nu = 0.4955$ in linear theory (cf. [61]). Meshes used for the geometry described above always have two elements in direction of the thickness for 3D simulations and various numbers of elements per side n_{el}, namely $n_{el} \in \{2, 4, 8, 16\}$, to determine the convergence behavior with mesh refinement (h-convergence). The reference and deformed configuration for a 3D mesh with $n_{el} = 16$ is shown in Figure 14.

The evaluation of this test is conducted for several sets of elements, whose convergence behavior of the top corner displacement $u = u_y$ with mesh refinement is shown in Fig. 15. The results for the first set of elements, which includes various standard elements, are plotted in Fig. 15a. Severe locking of the pure displacement based element H1 is the first and most obvious result gained from the plot. Due to shear and volumetric locking it exhibits poor coarse mesh accuracy as well as slow convergence behavior, demonstrating impressively why enhanced elements were introduced in the first place. All other elements perform similar to H1/E9 with slightly better results for coarse meshes exhibited by H1/E12T, HM1/E12T and HA1/E12T due too the 3 additional enhanced modes. Interestingly, H1/E12T, HM1/E12T and HA1/E12T also perform better than H1/E12, HM1/E12 and HA1/E12 (not shown in the diagrams), respectively.

The second plot, Fig. 15b, shows some elements based on the transpose of the Wilson-modes (40). It is included to compare the performance of the novel transformation, which uses the transpose inverse deformation gradient at the element centroid (35) for
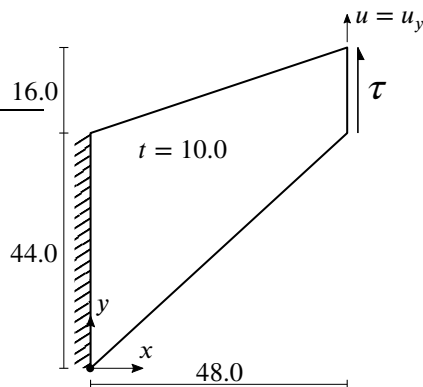
FIGURE 13 Geometry and boundary conditions for the Cooks membrane test.
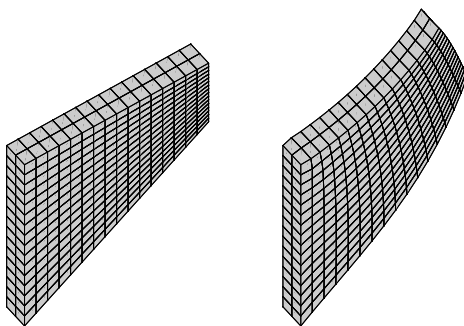

FIGURE 14 Deformed and undeformed configuration of Cooks membrane (3D). Plots generated with Q1/E9 element.

frame invariance, to standard EAS elements. Remarkably, element H1/E9T-F_0^{-T} with the newly proposed transformation performs 10.7% better for the coarsest mesh when compared to H1/E9T. There is even an improvement compared to HA1/E12T, even though H1/E9T-F_0^{-T} has three enhanced modes less. Note however, that in contrast to H1/E9T-F_0^{-T}, HA1/E12T is completely locking-free, which is advantageous in elasto-plastic tests (see[38]). The overall best performance in the cooks membrane test of all elements tested in the present work is furnished by element HA1/E12T-F_0^{-T}, which uses the newly proposed improved modification of the compatible deformations (28), the novel transformation (35) and 12 enhanced modes.

The final plots in Fig. 15c and 15d compare the performance of various transformations listed in (38). Note, that there are many transformations which yield the same result for specific choices of shape functions. Only the unique transformations are included in the plots for both the EAS element based on Wilson-modes (Fig. 15c) and transpose Wilson-modes (Fig. 15d), respectively. All other transformations are duplicates of the ones shown in Fig. 15, which can be proven with the information given in Remark 10 and also verified numerically. The most important result is that the standard transformation (38a) yields the best results for both types of shape functions. Furthermore, it is interesting that no transformation at all (38i) (elements H1/E9-$J_0(i)$ and H1/E9T-$J_0(i)$ i.e. original Wilson modes and transpose thereof in combination with transformation (38i)) performs better than using an inappropriate transformation. For the examined case, there is virtually no difference between using the Jacobian at the element centroid (18) and the average Jacobian (39) (compare H1/E9-$J_0(a)$ and H1/E9-$J_{avg}(a)$).

However, these results hold only for the special case of shape functions examined here. Other relations may be found for other shape functions than the Wilson-modes and the transpose thereof, which is why these tests should be repeated if novel modes for the enhanced field are proposed.
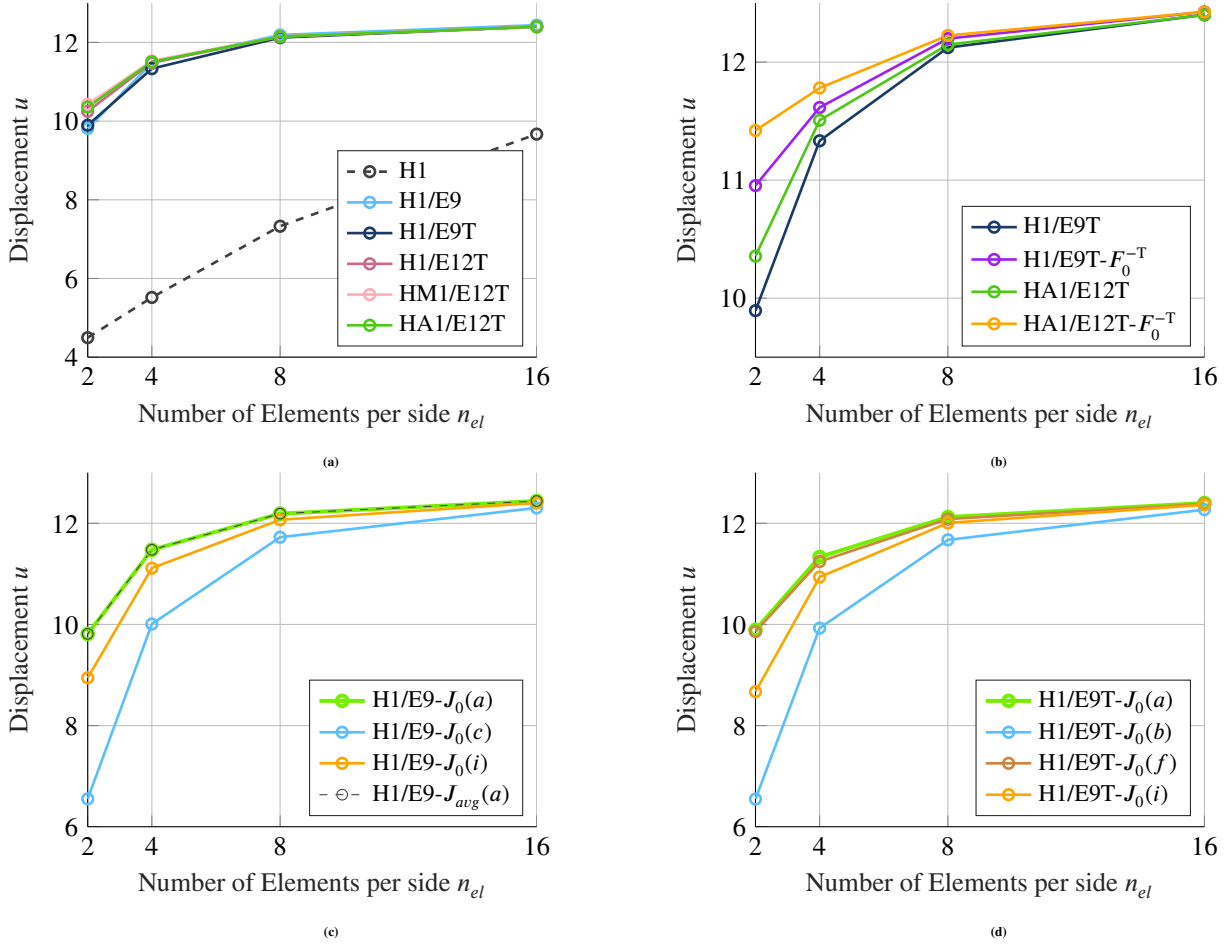
FIGURE 15 Cooks membrane test: convergence of top corner displacement u with mesh refinement. Various sets of 3D elements.

4 | CONCLUSION

First of all, we examined and compared shape functions previously used for the enhanced deformation gradient of the geometrically nonlinear EAS method and summarized their behavior in various tests. An important reproduced result is the by now well documented spurious hour-glassing instability of the EAS element based on the original Wilson-modes (cf. Section 3.4 and [41,43,19,22,26]). This spurious behavior can be avoided for the polyconvex hyperelastic materials considered here by using the transpose of the Wilson modes, which has been shown in previous works (cf. e.g. [19,22]). Moreover, we showed that the extra three enhanced modes introduced by Simo et al. [1] have little effect for the elastic problems considered here, even though they further reduce locking. For elasto-plastic problems however, this reduction of locking is crucial to compute correct limit loads (see [38]).

Secondly, we thoroughly investigated transformations between the reference and physical domain for the compatible and incompatible deformation gradient. We showed numerically and with a novel analytic proof, that the modified evaluation of the compatible deformation gradient presented by Simo et al. [1] (e.g. element HM1/E12) does not fulfill the patch test in generally distorted meshes (see also [21,34]). This makes the respective element unsuitable for general practical problems, where irregular meshes occur often due to mesh generators. This major drawback can be overcome with a novel approach we introduced in the present work. It relies on the evaluation of shape functions used for hourglass-stbilization introduced by Flanagan and Belytschko [47], which is employed here to modify the method of Simo et al. [1]. This novel approach has the advantage of maintaining the completely locking-free behavior of HM1/E12T for arbitrary meshes whilst curing the violation of the patch, what we also verified with an analytic proof.

Finally, the transformation of the enhanced deformation gradient is also thoroughly covered in the present work and several novel transformations are introduced and compared. Most remarkably is that element H1/E9T-F_0^{-T}, using an alternative transformation

motivated with the help of a curvilinear coordinate system (see Appendix A) to ensure frame invariance, yields superior coarse mesh accuracy compared to all previously introduced elements. Even HM1/E12T, which has 3 additional enhanced modes, performs worse than the element with the newly proposed transformation. Only elements HM1/E12T-F_0^{-T} and HA1/E12T-F_0^{-T}, which use the novel transformation as well, perform slightly better.

All in all, the results of the present work show that EAS elements using the transpose Wilson-modes can be successfully employed to simulate elastic solid mechanics problems. We especially recommend using the newly proposed elements H1/E9T-F_0^{-T} and HA1/E12T-F_0^{-T} due to their excellent behavior in the problems considered here.

However, the ultimate task of finding a generally applicable element requires elements also suitable for other geometries including shell structures and more importantly arbitrary materials. These issues are beyond the scope of the present work and should be investigated further.

Acknowledgement

☐

APPENDIX

A TRANSFORMATIONS OF THE ENHANCED DEFORMATION GRADIENT

This appendix elaborates upon the transformation of the enhanced deformation gradient treated in Section 2.2.2 with the help of a curvilinear coordinate system, which is introduced by reinterpreting the isoparametric coordinates $\mathbf{X}^{h,e}$ given in (9) as functions of $\boldsymbol{\xi} = \begin{bmatrix} \xi & \eta & \zeta \end{bmatrix}^T = \begin{bmatrix} \xi_1 & \xi_2 & \xi_3 \end{bmatrix}^T$. The covariant basis vectors of the reference configuration (see Fig. A1) of an element Ω_e are defined as

$$\mathbf{G}_i = \frac{\partial \mathbf{X}^{h,e}}{\partial \xi_i}, \qquad i = 1, 2, 3. \tag{A1}$$

Additionally, a cartesian basis $\{\mathbf{e}_i\}$ is introduced in the space of the reference element $\hat{\Omega}$. Corresponding to $\{\mathbf{G}_i\}$, a dual contravariant basis $\{\mathbf{G}^i\}$ is defined by $\mathbf{G}_i \cdot \mathbf{G}^j = \delta_i^j$. Finally, a spatial covariant basis $\{\mathbf{g}_i\}$ is defined analogously to (A1) by

$$\mathbf{g}_i = \frac{\partial \mathbf{x}^{h,e}}{\partial \xi_i}, \qquad i = 1, 2, 3, \tag{A2}$$

and is derived from the spatial configuration $\mathbf{x}^{h,e} = \boldsymbol{\varphi}^{h,e}$. The tangential maps[12] between the configurations are given by

$$\mathbf{F}_\varphi^{h,e} = \sum_{i=1}^3 \mathbf{g}_i \otimes \mathbf{G}^i, \qquad \mathbf{J}^{h,e} = \sum_{i=1}^3 \mathbf{G}_i \otimes \mathbf{e}^i, \qquad \mathbf{j}^{h,e} = \sum_{i=1}^3 \mathbf{g}_i \otimes \mathbf{e}^i, \tag{A3}$$

which denote the approximations of the deformation gradient and jacobians (material and spatial). They satisfy relation $\mathbf{j}^{h,e} = \mathbf{F}_\varphi^{h,e} \mathbf{J}^{h,e}$. Further useful relations between the bases are e.g.

$$\mathbf{g}_i = \mathbf{j}^{h,e} \mathbf{e}_i, \qquad \mathbf{G}_i = \mathbf{J}^{h,e} \mathbf{e}_i, \tag{A4a}$$

$$\mathbf{g}^i = (\mathbf{j}^{h,e})^{-T} \mathbf{e}^i, \quad \mathbf{G}^i = (\mathbf{J}^{h,e})^{-T} \mathbf{e}^i. \tag{A4b}$$

All transformations and bases are depicted in Fig. A1.

In the next step, we assume that the enhanced deformation gradient $\tilde{\mathbf{F}}^{h,e}$ has the same mixed co-/contravariant and two-field structure as the compatible deformation gradient $\mathbf{F}_\varphi^{h,e}$, which has the advantage, that frame-invariance is automatically implied. Thus we define

$$\tilde{\mathbf{F}}^{h,e} = \tilde{F}^i_{.j} \mathbf{g}_i \otimes \mathbf{G}^j \tag{A5}$$

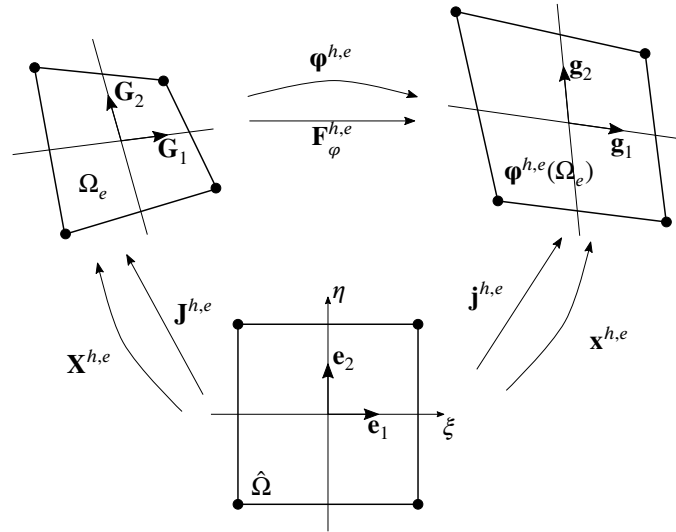[12]Tangential maps map infinitesimal line elements from one configuration to another.

FIGURE A1 Coordinate systems and transformations of an isoparametric quadrilateral 2D finite element Ω_e

where the summation convention applies and the index with dot in $\tilde{F}^i_{\cdot j}$ denotes the second index. Inserting from (A4) into the last equation yields

$$\tilde{\mathbf{F}}^{h,e} = \tilde{F}^i_{\cdot j}(\mathbf{j}^{h,e}\mathbf{e}_i) \otimes ((\mathbf{J}^{h,e})^{-\mathrm{T}}\mathbf{e}_j) = \mathbf{F}^{h,e}\mathbf{J}^{h,e}\left(\tilde{F}^i_{\cdot j}\mathbf{e}_i \otimes \mathbf{e}_j\right)(\mathbf{J}^{h,e})^{-1}, \tag{A6}$$

which describes the transformation of the enhanced field in the reference system $\tilde{\mathbb{F}} := \tilde{F}^i_{\cdot j}\mathbf{e}_i \otimes \mathbf{e}_j$ into the physical space and was first introduced by Simo et al. [1]. In essence[13], (A6) is the same as employing (38b) together with (34). Another possibility to define the enhanced field is the purely covariant version

$$\tilde{\mathbf{F}}^{h,e} = \tilde{F}_{ij}\mathbf{g}^i \otimes \mathbf{G}^j \tag{A7}$$

which gives a transformation rule similar to combination of (38a) and (35) given by

$$\tilde{\mathbf{F}}^{h,e} = (\mathbf{F}^{h,e})^{-\mathrm{T}}(\mathbf{J}^{h,e})^{-\mathrm{T}}\tilde{\mathbb{F}}(\mathbf{J}^{h,e})^{-1}. \tag{A8}$$

Note, that $\tilde{\mathbb{F}} = \tilde{F}^i_{\cdot j}\mathbf{e}_i \otimes \mathbf{e}_j = \tilde{F}_{ij}\mathbf{e}_i \otimes \mathbf{e}_j$ since $\{\mathbf{e}_i\}$ is cartesian. Furthermore, (A8) is also frame-invariant as described in Section 2.2.2. This consequent covariant approach has to the best knowledge of the authors never been used before. Instead, (38a) has often (see e.g. [22,16,26]) been used together with (34) which can be viewed as mixture of the approaches (A6) and (A8) and yields a simpler implementation. Interestingly, approach (A8) outperforms (A6) in some numerical experiments, which is shown in Section 3.7. Which version is best, also depends on the type of shape functions chosen for the enhanced field.

B ALTERNATIVE REPRESENTATION OF SHAPE FUNCTIONS

This Appendix covers the computation of the average gradient of shape functions within an element defined in (27). Furthermore, we compare the various alternative representations of the gradient of shape functions used for the compatible deformation gradient given in Section 2.2.1. In particular, we adress a part of the shape functions that is neglected by the use of the average gradient. Note, that this neglected part has no implications on the patch test and does not lead to rank deficiencies of skewed elements (cf. Belytschko and Bindemann [52]). Using the average gradient of shape functions is even necessary to fulfill the patch test for generally distorted elements in (a) the context of hourglass-stabilization (c.f. Belytschko et al. [51,52]) as well as for (b) the modification (28) of the gradient of shape functions used for the compatible deformation gradient in the present work (see Section 2.2.1 and Appendix C).

---

[13] Without considering the centroid evaluation and scaling with determinants, which is necessary to fulfill the patch test (see Section 2.4).

TABLE B1 Permutations of nodes for b_I^X, b_I^Y and b_I^Z

I	Permuted node numbers							
1	1	2	3	4	5	6	7	8
2	2	3	4	1	6	7	8	5
3	3	4	1	2	7	8	5	6
4	4	1	2	3	8	5	6	7
5	5	8	7	6	1	4	3	2
6	6	5	8	7	2	1	4	3
7	7	6	5	8	3	2	1	4
8	8	7	6	5	4	3	2	1

B.1 Average gradient of shape functions

The analytic method to compute the average gradient of shape functions, which is outlined here, was developed by Flanagan and Belytschko[47] and can also be found e.g. in[51].

In a first step, the reference nodal coordinates $\mathbf{X}_I^e = \begin{bmatrix} X_I^e & Y_I^e & Z_I^e \end{bmatrix}^{\mathrm{T}}$, $I = 1, \dots, 8$ are used to compute values b_I^X, b_I^Y and b_I^Z. They are given e.g. for $I = 1$ by

$$
\begin{aligned}
b_1^X = \tfrac{1}{12}\big(\ & Y_2^e((Z_6^e - Z_3^e) - (Z_4^e - Z_5^e)) + Y_3^e(Z_2^e - Z_4^e) + \\
& Y_4^e((Z_3^e - Z_8^e) - (Z_5^e - Z_2^e)) + Y_6^e(Z_5^e - Z_2^e) + \\
& Y_5^e((Z_8^e - Z_6^e) - (Z_2^e - Z_4^e)) + Y_8^e(Z_4^e - Z_5^e) \ \big),
\end{aligned}
\tag{B9a}
$$

$$
\begin{aligned}
b_1^Y = \tfrac{1}{12}\big(\ & Z_2^e((X_6^e - X_3^e) - (X_4^e - X_5^e)) + Z_3^e(X_2^e - X_4^e) + \\
& Z_4^e((X_3^e - X_8^e) - (X_5^e - X_2^e)) + Z_6^e(X_5^e - X_2^e) + \\
& Z_5^e((X_8^e - X_6^e) - (X_2^e - X_4^e)) + Z_8^e(X_4^e - X_5^e) \ \big),
\end{aligned}
\tag{B9b}
$$

$$
\begin{aligned}
b_1^Z = \tfrac{1}{12}\big(\ & X_2^e((Y_6^e - Y_3^e) - (Y_4^e - Y_5^e)) + X_3^e(Y_2^e - Y_4^e) + \\
& X_4^e((Y_3^e - Y_8^e) - (Y_5^e - Y_2^e)) + X_6^e(Y_5^e - Y_2^e) + \\
& X_5^e((Y_8^e - Y_6^e) - (Y_2^e - Y_4^e)) + X_8^e(Y_4^e - Y_5^e) \ \big).
\end{aligned}
\tag{B9c}
$$

Note, that only the coordinates X_I^e, Y_I^e, Z_I^e but not the node numbers I change in the right hand side of above equations. The values of b_I^X, b_I^Y and b_I^Z for $I \neq 1$ can be computed by permuting the nodes in (B9) according to Table B1.

In a next step the exact volume of element Ω_e is computed from (B9) via relation

$$
V = \sum_{I=1}^{8} b_I^X X_I^e.
\tag{B10}
$$

Note, that using b_I^Y and Y_I^e or b_I^Z and Z_I^e yields the same result. With (B9) and (B10) at hand, the final relation to compute (27) is

$$
\bar{\nabla}_{\mathbf{X}} N_I = \frac{1}{V} \begin{bmatrix} b_I^X \\ b_I^Y \\ b_I^Z \end{bmatrix} \qquad I = 1, \dots, 8.
\tag{B11}
$$

B.2 Comparison of alternative shape function representations

In the following we examine two representations of the tri-linear shape functions to quantify the inaccuracy introduced by the use of the average gradient of shape functions. We start by noting that the standard form of the tri-linear shape functions in the isoparametric space given in (10) can alternatively be expressed in vector form (e.g. Wriggers[2])

$$
\mathbf{N} = \frac{1}{8}\mathbf{a}^0 + \frac{1}{8}\sum_{I=1}^{3} \mathbf{a}^I \xi_I + \frac{1}{8}\sum_{A=1}^{4} \mathbf{h}^A H_A(\boldsymbol{\xi}).
\tag{B12}
$$

Therein, $H_A(\xi)$ and $\mathbf{h}^A$, $A = 1, \ldots, 4$, are defined in (19) and (23), respectively. Moreover, the vectors $\mathbf{a}^0$ and $\mathbf{a}^I$, $I = 1, \ldots, 3$, are given by

$$
\begin{aligned}
\mathbf{a}^0 &= \begin{bmatrix} 1 & 1 & 1 & 1 & 1 & 1 & 1 & 1 \end{bmatrix}^{\mathrm{T}}, \\
\mathbf{a}^1 &= \begin{bmatrix} -1 & 1 & 1 & -1 & -1 & 1 & 1 & -1 \end{bmatrix}^{\mathrm{T}}, \\
\mathbf{a}^2 &= \begin{bmatrix} -1 & -1 & 1 & 1 & -1 & -1 & 1 & 1 \end{bmatrix}^{\mathrm{T}}, \\
\mathbf{a}^3 &= \begin{bmatrix} -1 & -1 & -1 & -1 & 1 & 1 & 1 & 1 \end{bmatrix}^{\mathrm{T}}.
\end{aligned}
\tag{B13}
$$

B.2.1 Standard Taylor series representation of the shape functions

The Taylor series of the shape functions in the physical frame at the element centroid $\mathbf{X}_0 = \sum_{I=1}^{8} N_I(\xi = 0)\mathbf{X}_I^e = \frac{1}{8}\tilde{\mathbf{X}}^e \mathbf{a}^0$ (with $\tilde{\mathbf{X}}^e$ defined in (22)) up to the linear part is given by

$$
\mathbf{N}(\mathbf{X}^e) = \mathbf{N}(\mathbf{X}^e = \mathbf{X}_0) + \left.\frac{\partial \mathbf{N}}{\partial \mathbf{X}^e}\right|_{\mathbf{X}^e = \mathbf{X}_0} (\mathbf{X}^e - \mathbf{X}_0) + \mathbf{N}_\gamma(\mathbf{X}^e).
\tag{B14}
$$

Therein, the first two terms on the right-hand side furnish the linear part $\mathbf{N}_{\text{lin}}$, while $\mathbf{N}_\gamma$ denotes the residual term. Taking a closer look at the linear part reveals

$$
\begin{aligned}
\mathbf{N}_{\text{lin}} &= \mathbf{N}(\mathbf{X}^e = \mathbf{X}_0) + \left.\frac{\partial \mathbf{N}}{\partial \mathbf{X}^e}\right|_{\mathbf{X}^e = \mathbf{X}_0} (\mathbf{X}^e - \mathbf{X}_0) = \frac{1}{8}\mathbf{a}^0 + (\nabla_0 \mathbf{N})^{\mathrm{T}}\left(\tilde{\mathbf{X}}^e \mathbf{N} - \frac{1}{8}\tilde{\mathbf{X}}^e \mathbf{a}^0\right) \\
&= \frac{1}{8}\mathbf{a}^0 + (\nabla_{\xi = 0}\mathbf{N})^{\mathrm{T}}\mathbf{J}_0^{-1}\tilde{\mathbf{X}}^e \frac{1}{8}\begin{bmatrix} \mathbf{a}^1 & \mathbf{a}^2 & \mathbf{a}^3 \end{bmatrix}\xi + \frac{1}{8}(\nabla_0 \mathbf{N})^{\mathrm{T}}\tilde{\mathbf{X}}^e \sum_{A=1}^{4}\mathbf{h}^A H_A(\xi) \\
&= \frac{1}{8}\mathbf{a}^0 + \sum_{I=1}^{3}\mathbf{a}^I \xi_I + \frac{1}{8}(\nabla_0 \mathbf{N})^{\mathrm{T}}\tilde{\mathbf{X}}^e \sum_{A=1}^{4}\mathbf{h}^A H_A(\xi),
\end{aligned}
\tag{B15}
$$

where use has been made of relation

$$
\nabla_{\xi = 0}\mathbf{N} = \frac{1}{8}\begin{bmatrix} \mathbf{a}_1^{\mathrm{T}} \\ \mathbf{a}_2^{\mathrm{T}} \\ \mathbf{a}_3^{\mathrm{T}} \end{bmatrix}.
\tag{B16}
$$

as well as $\left.\frac{\partial \mathbf{N}}{\partial \mathbf{X}}\right|_{\mathbf{X}^e = \mathbf{X}_0} = (\nabla_{\xi = 0}\mathbf{N})^{\mathrm{T}}\mathbf{J}_0^{-1}$ and $\mathbf{J}_0 = \tilde{\mathbf{X}}^e(\nabla_{\xi = 0}\mathbf{N})^{\mathrm{T}}$. The latter two relations can be established from (17), (13a) and (18).

In view of (B14) and (B15) the residual part $\mathbf{N}_\gamma$ finally assumes the simple form

$$
\mathbf{N}_\gamma = \mathbf{N} - \mathbf{N}_{\text{lin}} = \sum_{A=1}^{4}\frac{1}{8}\left[\mathbf{h}^A - (\nabla_0 \mathbf{N})^{\mathrm{T}}\tilde{\mathbf{X}}^e \mathbf{h}^A\right] H_A(\xi) = \sum_{A=1}^{4}\boldsymbol{\gamma}^A H_A(\xi)
\tag{B17}
$$

where the gamma-stabilization vectors (20) occur.

B.2.2 Using the average gradient of shape functions

The gradient of shape functions at the element centroid in (B14) can be replaced with the average gradient of shape functions $\overline{\nabla}_{\mathbf{X}}\mathbf{N}$ defined in (27) and thoroughly described in Section B.1. This yields

$$
\mathbf{N}(\mathbf{X}^e) = \mathbf{N}(\mathbf{X}^e = \mathbf{X}_0) + \left(\overline{\nabla}_{\mathbf{X}}\mathbf{N}\right)^{\mathrm{T}}(\mathbf{X}^e - \mathbf{X}_0) + \hat{\mathbf{N}}_\gamma(\mathbf{X}^e).
\tag{B18}
$$

Note, that this is not a real Taylor-series since the mean-value theorem does not hold for vector-valued functions and thus in general no $\mathbf{X}^*$ exists at which $\overline{\nabla}_{\mathbf{X}}\mathbf{N} = \nabla_{\mathbf{X}}N(\mathbf{X}^*)$ holds. The implications of this are described subsequently.

The linear part $\mathbf{N}_{\text{lin}}$ cannot be simplified to the same extent as in the previous Section since the jacobians cannot be canceled out

as in (B15). In fact with the same steps as before the remaining residual part is

$$
\hat{\mathbf{N}}_\gamma = \sum_{J=1}^{3} \frac{1}{8} \left[\mathbf{a}^J - (\bar{\nabla}_{\mathbf{X}} \mathbf{N})^{\mathrm{T}} \tilde{\mathbf{X}}^e \mathbf{a}^J \right] \xi_J + \sum_{A=1}^{4} \frac{1}{8} \left[\mathbf{h}^A - (\bar{\nabla}_{\mathbf{X}} \mathbf{N})^{\mathrm{T}} \tilde{\mathbf{X}}^e \mathbf{h}^A \right] H_A(\boldsymbol{\xi})
$$
$$
= \sum_{J=1}^{3} \hat{\boldsymbol{\beta}}^J \xi_J + \sum_{A=1}^{4} \hat{\boldsymbol{\gamma}}^A H_A(\boldsymbol{\xi}), \tag{B19}
$$

where we introduced

$$
\hat{\boldsymbol{\beta}}^J = \frac{1}{8} \left[\mathbf{a}^J - (\bar{\nabla}_{\mathbf{X}} \mathbf{N})^{\mathrm{T}} \tilde{\mathbf{X}}^e \mathbf{a}^J \right] \qquad \text{and} \qquad \hat{\boldsymbol{\gamma}}^A = \frac{1}{8} \left[\mathbf{h}^A - (\bar{\nabla}_{\mathbf{X}} \mathbf{N})^{\mathrm{T}} \tilde{\mathbf{X}}^e \mathbf{h}^A \right]. \tag{B20}
$$

In contrast to (B17) there are two residual parts in (B19). The second part containing $\hat{\boldsymbol{\gamma}}^A$ is almost the same as (B17) with only the gradient of shape functions exchanged in the definition of the gamma-stabilization vector. The first one is linear and has a similar structure. As stated in Belytschko and Bindemann[52] this part is usually neglected for hourglass stabilization techniques based on the average gradient of shape functions and is also neglected in the present work (see (28)). However, this has no major impact on the accuracy and does not lead to insufficiently rich approximation spaces (cf.[52]).

Remark 11. In the case of a parallelepiped it is obvious from definitions (27) and (17) that $\bar{\nabla}_{\mathbf{X}} N_I \equiv \nabla_{\mathbf{0}} N_I$ holds since the Jacobian is constant for such a geometry. Consequently, the vectors $\hat{\boldsymbol{\beta}}^J$ and therefore the surplus part vanish, which can be shown with similar steps as in (B15).

C PATCH TEST AND THE COMPATIBLE DEFORMATION GRADIENT

This appendix elaborates upon the patch test criterion for the compatible deformation gradient. In particular, we prove that the element proposed by Simo et al.[1] does not fulfill the patch test for arbitrary meshes while the newly proposed method (28) always fulfills it. We start by considering the homogeneous deformation

$$
\boldsymbol{\varphi} = \mathbf{F}_0 \mathbf{X} + \mathbf{c} \tag{C21}
$$

with constant tensor $\mathbf{F}_0 \in \mathbb{R}^{3\times3}$ and vector $\mathbf{c} \in \mathbb{R}^3$, which implies a constant deformation gradient[14]

$$
\mathbf{F} = \frac{\partial \boldsymbol{\varphi}}{\partial \mathbf{X}} = \mathbf{F}_0. \tag{C22}
$$

The patch test criterion requires, that states of constant strain are reproduced exactly by the numerical method. Thus, under a state of homogeneous deformation with nodal deformations $\boldsymbol{\varphi}_I^e = \mathbf{F}_0 \mathbf{X}_I^e + \mathbf{c}$ two conditions need to be met:

- Firstly, $\mathbf{F}^{h,e} \equiv \mathbf{F}_0$ has to hold and

- secondly, it is necessary that the finite element residual is equivalent to the analytic solution, which is quite difficult to prove from scratch. However, the condition can easily be checked by comparison with the isoparametric element, since that element always fulfills the patch test.

In the following we examine these requirements for all three versions of the compatible deformation gradient considered in the present work. Namely, we study the isoparametric concept with standard gradient of shape functions (15) (which is well-known to fulfill the patch test), the modification proposed by Simo et al. using (16) and the novel improved version based on (28). Furthermore, only the 3D case is considered subsequently since the 2D case is trivial (see Remark 6).

C.1 Approximation of the deformation gradient

In this Section we will show that requirement $\mathbf{F}^{h,e} = \mathbf{F}_0$ is fulfilled by all three versions of the deformation gradient considered in this work. We start with the isoparametric concept, where in view of (14), (15) and (13) we get for the compatible deformation

---

[14]In general: $\mathbf{F} = $ const. $\Leftrightarrow \boldsymbol{\varphi} = $ homogeneous (cf. Gonzales and Stuart[64])

gradient

$$\mathbf{F}^{h,e} = \sum_{I=1}^{8} \boldsymbol{\varphi}_I^e \otimes \nabla_{\mathbf{X}} N_I = \mathbf{F}_0 \sum_{I=1}^{8} \left(\mathbf{X}_I^e \otimes \nabla_{\boldsymbol{\xi}} N_I \right) (\mathbf{J}^{h,e})^{-1} + \mathbf{c} \otimes \nabla_{\boldsymbol{\xi}} \sum_{I=1}^{8} \left(N_I \right) (\mathbf{J}^{h,e})^{-1}$$

$$= \mathbf{F}_0 \mathbf{J}^{h,e} (\mathbf{J}^{h,e})^{-1} + \mathbf{c} \otimes \nabla_{\boldsymbol{\xi}} (1) (\mathbf{J}^{h,e})^{-1} = \mathbf{F}_0 \tag{C23}$$

which is the desired result. If we use the modified gradient (16) instead of (15) the proof gets more complicated. However, with similar steps as above we get

$$\mathbf{F}^{h,e} = \sum_{I=1}^{8} \boldsymbol{\varphi}_I^e \otimes \widetilde{\nabla}_{\mathbf{X}} N_I = \mathbf{F}_0 \sum_{I=1}^{8} \left(\mathbf{X}_I^e \otimes \widetilde{\nabla}_{\mathbf{X}} N_I \right) + \mathbf{c} \otimes \sum_{I=1}^{8} \bar{\nabla}_{\mathbf{X}} N_I$$

$$= \mathbf{F}_0 \sum_{I=1}^{8} \left[\mathbf{X}_I^e \otimes \left(\nabla_{\boldsymbol{\xi}} N_I |_{\boldsymbol{\xi} = \mathbf{0}} + \sum_{A=1}^{4} \frac{j_0}{j^{h,e}} \nabla_{\boldsymbol{\xi}} H_A \gamma_I^A \right) \right] \mathbf{J}_0^{-1} \tag{C24}$$

$$= \mathbf{F}_0 + \mathbf{F}_0 \sum_{I=1}^{8} \left[\mathbf{X}_I^e \otimes \sum_{A=1}^{4} \frac{j_0}{j^{h,e}} \nabla_{\boldsymbol{\xi}} H_A \gamma_I^A \right] \mathbf{J}_0^{-1}$$

where use has been made of identity

$$\sum_{I=1}^{8} \widetilde{\nabla}_{\mathbf{X}} N_I = \sum_{I=1}^{8} \nabla_{\mathbf{0}} N_I + \frac{j_0}{j^{h,e}} \mathbf{J}_0^{-\mathrm{T}} \sum_{I=1}^{8} \sum_{A=1}^{4} \nabla_{\boldsymbol{\xi}} H_A \gamma_I^A$$

$$= \frac{j_0}{8 j^{h,e}} \mathbf{J}_0^{-\mathrm{T}} \left[\sum_{A=1}^{4} \sum_{J=1}^{8} \nabla_{\boldsymbol{\xi}} H_A \left(h_J^A \mathbf{X}_J^e \cdot \sum_{I=1}^{8} \nabla_{\mathbf{0}} N_I \right) + \sum_{I=1}^{8} \sum_{A=1}^{4} \nabla_{\boldsymbol{\xi}} H_A h_I^A \right] = \mathbf{0}. \tag{C25}$$

Note, that the last equation can be established with help of $\sum_{I=1}^{8} \nabla_{\boldsymbol{\xi}} N_I = \mathbf{0}$ and definition (20) of the gamma stabilization vectors. Since the desired result is $\mathbf{F}^{h,e} = \mathbf{F}_0$, the second term in the last line of (C24) has to vanish. With definition (20) of the gamma stabilization vectors we get after basic, but lengthy tensor algebra.

$$\mathbf{F}_0 \sum_{I=1}^{8} \left[\mathbf{X}_I^e \otimes \sum_{A=1}^{4} \frac{j_0}{j^{h,e}} \nabla_{\boldsymbol{\xi}} H_A \gamma_I^A \right] \mathbf{J}_0^{-1} = \frac{1}{8} \mathbf{F}_0 \frac{j_0}{j^{h,e}} \sum_{I=1}^{8} \sum_{A=1}^{4} \left(\mathbf{X}_I^e h_I^A \otimes \nabla_{\boldsymbol{\xi}} H_A - \mathbf{J}_0 \mathbf{J}_0^{-1} \mathbf{X}_I^e h_I^A \otimes \nabla_{\boldsymbol{\xi}} H_A \right) = \mathbf{0}. \tag{C26}$$

Thus, $\mathbf{F}^{h,e} = \mathbf{F}_0$ is established for the modification of Simo et al.[1] as well. For the novel, improved version of that modification given in (28) we start by noting relations

$$\sum_{I=1}^{8} \mathbf{X}_I^e \otimes \bar{\nabla}_{\mathbf{X}} N_I = \mathbf{I} \qquad \text{and} \qquad \sum_{I=1}^{8} \bar{\nabla}_{\mathbf{X}} N_I = \mathbf{0} \tag{C27}$$

which follow, albeit with tedious algebra, from the definition of the average gradient of shape functions (27). A proof of the last identities can e.g. be found in Flanagan and Belytschko[47]. With this information at hand and similar steps as above we get

$$\mathbf{F}^{h,e} = \sum_{I=1}^{8} \boldsymbol{\varphi}_I^e \otimes \hat{\nabla}_{\mathbf{X}} N_I = \mathbf{F}_0 \sum_{I=1}^{8} \left(\mathbf{X}_I^e \otimes \hat{\nabla}_{\mathbf{X}} N_I \right) + \mathbf{c} \otimes \sum_{I=1}^{8} \hat{\nabla}_{\mathbf{X}} N_I = \mathbf{F}_0. \tag{C28}$$

Thus, we have shown that criterion $\mathbf{F}^{h,e} \equiv \mathbf{F}_0$ holds for all versions of the compatible deformation gradient considered.

C.2 Finite element residual

The result of the previous section shows that the same constant state of strain is obtained regardless of the gradient of shape functions used. Together with the assumption of a homogeneous material this yields analogously the same constant stresses $\mathbf{P}^{h,e} = \mathbf{P}_0$ for all three versions. With this information at hand, the finite element residual of one finite element with isoparametric formulation using the work-conjugate measures $\mathbf{P}$ and $\mathbf{F}$ is given by

$$\delta_{\boldsymbol{\varphi}} \Pi = \int_{\Omega_e} \mathbf{P}^{h,e} : \delta_{\boldsymbol{\varphi}} \mathbf{F}^{h,e} \, \mathrm{d}V = \sum_{I=1}^{8} \mathbf{P}_0 \delta \boldsymbol{\varphi}_I \cdot \int_{\Omega_e} \nabla_{\mathbf{X}} N_I \, \mathrm{d}V. \tag{C29}$$

Note, that the equation above is exact, in the sense that it coincides with the analytic solution, because the isoparametric element fulfills the patch test. In the following we compare the residuals of the other two versions of the deformation gradient to that

result.

Starting with the modification (16) of the gradient of shape functions by Simo et al. we get with $\int_{\hat{\Omega}} \nabla_\xi H_A \, d\hat{\Omega} = \mathbf{0}, \ A = 1, \dots, 4$ and straightforward steps

$$
\begin{aligned}
\delta_{\boldsymbol{\varphi}} \tilde{\Pi} &= \sum_{I=1}^{8} \mathbf{P}_0 \delta \boldsymbol{\varphi}_I \cdot \int_{\Omega_e} \widetilde{\nabla}_{\mathbf{X}} N_I \, dV = \sum_{I=1}^{8} \mathbf{P}_0 \delta \boldsymbol{\varphi}_I \cdot \left[\int_{\Omega_e} \nabla_0 N_I \, dV + j_0 \mathbf{J_0}^{-\mathrm{T}} \sum_{A=1}^{4} \int_{\hat{\Omega}} \frac{1}{j^{h,e}} \nabla_\xi H_A j^{h,e} \, d\hat{\Omega} \, \gamma_I^A \right] \\
&= \sum_{I=1}^{8} \mathbf{P}_0 \delta \boldsymbol{\varphi}_I \cdot \int_{\Omega_e} \nabla_0 N_I \, dV.
\end{aligned}
\tag{C30}
$$

Since (C29) and (C30) are in general not the same, the patch test is not fulfilled for generally distorted meshes. However, in case of a initially parallelepiped-shaped element $\int_{\Omega_e} \nabla_0 N_I \, dV \equiv \int_{\Omega_e} \nabla_{\mathbf{X}} N_I \, dV$ holds and the patch test is therefore fulfilled in that case. More favorably is the behavior of the improved version of the modification by Simo et al. given in (28). With definition (27) the residual reads

$$
\begin{aligned}
\delta_{\boldsymbol{\varphi}} \tilde{\Pi} &= \sum_{I=1}^{8} \mathbf{P}_0 \delta \boldsymbol{\varphi}_I \cdot \int_{\Omega_e} \hat{\nabla}_{\mathbf{X}} N_I \, dV = \sum_{I=1}^{8} \mathbf{P}_0 \delta \boldsymbol{\varphi}_I \cdot \left[\frac{1}{V} \int_{\Omega_e} \nabla_{\mathbf{X}} N_I \, dV \int_{\Omega_e} dV + j_0 \mathbf{J_0}^{-\mathrm{T}} \sum_{A=1}^{4} \int_{\hat{\Omega}} \frac{1}{j^{h,e}} \nabla_\xi H_A j^{h,e} \, d\hat{\Omega} \, \hat{\gamma}_I^A \right] \\
&= \sum_{I=1}^{8} \mathbf{P}_0 \delta \boldsymbol{\varphi}_I \cdot \int_{\Omega_e} \nabla_{\mathbf{X}} N_I \, dV.
\end{aligned}
\tag{C31}
$$

which is exactly the same as (C29). Thus, the patch test is fulfilled for arbitrary initial element shapes if the novel approach presented in this work is used.

References

1. Simo JC, Armero F, Taylor RL. Improved Versions of Assumed Enhanced Strain Tri-Linear Elements for 3D Finite Deformation Problems. *Comput. Methods Appl. Mech. Engrg.* 1993; 110(3-4): 359-386. doi: 10.1016/0045-7825(93)90215-J

2. Wriggers P. *Nonlinear Finite Element Methods*. Berlin; Heidelberg: Springer . 2008

3. Simo JC, Rifai MS. A Class of Mixed Assumed Strain Methods and the Method of Incompatible Modes. *Int. J. Numer. Meth. Engng.* 1990; 29(8): 1595-1638. doi: 10.1002/nme.1620290802

4. Simo JC, Armero F. Geometrically Non-Linear Enhanced Strain Mixed Methods and the Method of Incompatible Modes. *Int. J. Numer. Meth. Engng.* 1992; 33(7): 1413-1449. doi: 10.1002/nme.1620330705

5. Washizu K. *Variational Methods in Elasticity and Plasticity*. Elsevier Science Limited . 1982.

6. MacNeal RH. A Theorem Regarding the Locking of Tapered Four-Noded Membrane Elements. *International Journal for Numerical Methods in Engineering* 1987; 24(9): 1793-1799. doi: 10.1002/nme.1620240913

7. MacNeal RH. On the Limits of Finite Element Perfectability. *International Journal for Numerical Methods in Engineering* 1992; 35(8): 1589-1601. doi: 10.1002/nme.1620350804

8. Wilson EL, Taylor RL, Doherty WP, Ghaboussi J. Incompatible Displacement Models. In: Fenves SJ, Perrone N, Robinson AR., eds. *Numerical and Computer Methods in Structural Mechanics* New York: Elsevier. 1973 (pp. 43–57)

9. Taylor RL, Beresford PJ, Wilson EL. A Non-Conforming Element for Stress Analysis. *Int. J. Numer. Meth. Engng.* 1976; 10(6): 1211-1219. doi: 10.1002/nme.1620100602

10. Bischoff M, Romero I. A Generalization of the Method of Incompatible Modes. *Int. J. Numer. Meth. Engng.* 2007; 69(9): 1851-1868. doi: 10.1002/nme.1830

11. Büchter N, Ramm E, Roehl D. Three-Dimensional Extension of Non-Linear Shell Formulation Based on the Enhanced Assumed Strain Concept. *Int. J. Numer. Meth. Engng.* 1994; 37(15): 2551-2568. doi: 10.1002/nme.1620371504

12. Betsch P, Gruttmann F, Stein E. A 4-Node Finite Shell Element for the Implementation of General Hyperelastic 3D-Elasticity at Finite Strains. *Comput. Methods Appl. Mech. Engrg.* 1996; 130(1): 57-79. doi: 10.1016/0045-7825(95)00920-5

13. Andelfinger U, Ramm E. EAS-Elements for Two-Dimensional, Three-Dimensional, Plate and Shell Structures and Their Equivalence to HR-Elements. *Int. J. Numer. Meth. Engng.* 1993; 36(8): 1311-1337. doi: 10.1002/nme.1620360805

14. Armero F, Linder C. New Finite Elements with Embedded Strong Discontinuities in the Finite Deformation Range. *Comput. Methods Appl. Mech. Engrg.* 2008; 197(33-40): 3138-3170. doi: 10.1016/j.cma.2008.02.021

15. Linder C, Armero F. Finite Elements with Embedded Strong Discontinuities for the Modeling of Failure in Solids. *Int. J. Numer. Meth. Engng.* 2007; 72(12): 1391-1433. doi: 10.1002/nme.2042

16. Krischok A, Linder C. On the Enhancement of Low-Order Mixed Finite Element Methods for the Large Deformation Analysis of Diffusion in Solids. *Int. J. Numer. Meth. Engng.* 2016; 106(4): 278-297. doi: 10.1002/nme.5120

17. Miehe C. Aspects of the Formulation and Finite Element Implementation of Large Strain Isotropic Elasticity. *Int. J. Numer. Meth. Engng.* 1994; 37(12): 1981-2004. doi: 10.1002/nme.1620371202

18. Crisfield MA, Moita GF, Jelenić G, Lyons LPR. Enhanced Lower-Order Element Formulations for Large Strains. *Computational Mechanics* 1995; 17(1): 62-73. doi: 10.1007/BF00356479

19. Korelc J, Wriggers P. Consistent Gradient Formulation for a Stable Enhanced Strain Method for Large Deformations. *Engineering Computations* 1996; 13(1): 103-123. doi: 10.1108/02644409610111001

20. Korelc J, Wriggers P. An Efficient 3D Enhanced Strain Element with Taylor Expansion of the Shape Functions. *Computational Mechanics* 1996; 19(2): 30-40. doi: 10.1007/BF02757781

21. Wriggers P, Korelc J. On Enhanced Strain Methods for Small and Finite Deformations of Solids. *Computational Mechanics* 1996; 18(6): 413-428. doi: 10.1007/BF00350250

22. Glaser S, Armero F. On the Formulation of Enhanced Strain Finite Elements in Finite Deformations. *Engineering Computations* 1997; 14(7): 759-791. doi: 10.1108/02644409710188664

23. Klinkel S, Wagner W. A Geometrical Non-Linear Brick Element Based on the EAS-Method. *Int. J. Numer. Meth. Engng.* 1997; 40(24): 4529-4545. doi: 10.1002/(SICI)1097-0207(19971230)40:24<4529::AID-NME271>3.0.CO;2-I

24. Korelc J, Wriggers P. Improved Enhanced Strain Four-Node Element with Taylor Expansion of the Shape Functions. *Int. J. Numer. Meth. Engng.* 1997; 40(3): 407-421. doi: 10.1002/(SICI)1097-0207(19970215)40:3<407::AID-NME70>3.0.CO;2-P

25. Sprenger W, Wagner W. On the Formulation of Geometrically Nonlinear 3D-Rebar-Elements Using the Enhanced Assumed Strain Method. *Engineering Structures* 1999; 21(3): 209-218. doi: 10.1016/S0141-0296(97)00182-X

26. Armero F. On the Locking and Stability of Finite Elements in Finite Deformation Plane Strain Problems. *Computers & Structures* 2000; 75(3): 261-290. doi: 10.1016/s0045-7949(99)00136-4

27. Kasper EP, Taylor RL. A Mixed-Enhanced Strain Method. Part I: Geometrically Linear Problems. *Computers & Structures* 2000; 75(3): 237-250. doi: 10.1016/S0045-7949(99)00134-0

28. Kasper EP, Taylor RL. A Mixed-Enhanced Strain Method. Part II: Geometrically Nonlinear Problems. *Computers & Structures* 2000; 75(3): 251-260. doi: 10.1016/S0045-7949(99)00135-2

29. Reese S, Wriggers P. A Stabilization Technique to Avoid Hourglassing in Finite Elasticity. *Int. J. Numer. Meth. Engng.* 2000; 48(1): 79-109. doi: 10.1002/(SICI)1097-0207(20000510)48:1<79::AID-NME869>3.0.CO;2-D

30. Wall WA, Bischoff M, Ramm E. A Deformation Dependent Stabilization Technique, Exemplified by EAS Elements at Large Strains. *Comput. Methods Appl. Mech. Engrg.* 2000; 188(4): 859-871. doi: 10.1016/S0045-7825(99)00365-5

31. Reese S. On a Consistent Hourglass Stabilization Technique to Treat Large Inelastic Deformations and Thermo-Mechanical Coupling in Plane Strain Problems. *Int. J. Numer. Meth. Engng.* 2003; 57(8): 1095-1127. doi: 10.1002/nme.719

32. Auricchio F, Beirão da Veiga L, Lovadina C, Reali A. A Stability Study of Some Mixed Finite Elements for Large Deformation Elasticity Problems. *Comput. Methods Appl. Mech. Engrg.* 2005; 194(9-11): 1075-1092. doi: 10.1016/j.cma.2004.06.014

33. Auricchio F, Beirão da Veiga L, Lovadina C, Reali A. Stability of Some Finite Element Methods for Finite Elasticity Problems. In: Carstensen C, Wriggers P. , eds. *Mixed Finite Element Technologies*. 509 of *CISM International Centre for Mechanical Sciences*. Vienna: Springer Vienna. 2009 (pp. 179-206)

34. Müller-Hoeppe DS, Löhnert S, Wriggers P. A Finite Deformation Brick Element with Inhomogeneous Mode Enhancement. *Int. J. Numer. Meth. Engng.* 2009; 78(10): 1164-1187. doi: 10.1002/nme.2523

35. Korelc J, Šolinc U, Wriggers P. An Improved EAS Brick Element for Finite Deformation. *Computational Mechanics* 2010; 46(4): 641-659. doi: 10.1007/s00466-010-0506-0

36. Ten Eyck A, Lew A. An Adaptive Stabilization Strategy for Enhanced Strain Methods in Non-Linear Elasticity. *Int. J. Numer. Meth. Engng.* 2010; 81(11): 1387-1416. doi: 10.1002/nme.2734

37. Sussman T, Bathe KJ. Spurious Modes in Geometrically Nonlinear Small Displacement Finite Elements with Incompatible Modes. *Computers & Structures* 2014; 140: 14-22. doi: 10.1016/j.compstruc.2014.04.004

38. Andelfinger U, Ramm E, Roehl D. 2D and 3D Enhanced Assumed Strain Elements and Their Application in Plasticity. In: Owen DRJ, Oñate E, Hinton E., eds. *Proc. of the Third International Conference on Computational Plasticity (Complas). Fundamentals and Applications*; 1992; Barcelona, Spain.

39. Reddy BD, Simo JC. Stability and Convergence of a Class of Enhanced Strain Methods. *SIAM J. Numer. Anal.* 1995; 32(6): 1705-1728. doi: 10.1137/0732077

40. Arunakirinathar K, Reddy BD. Further Results for Enhanced Strain Methods with Isoparametric Elements. *Comput. Methods Appl. Mech. Engrg.* 1995; 127(1): 127-143. doi: 10.1016/0045-7825(95)00845-0

41. Wriggers P, Reese S. A Note on Enhanced Strain Methods for Large Deformations. *Comput. Methods Appl. Mech. Engrg.* 1996; 135(3-4): 201-209. doi: 10.1016/0045-7825(96)01037-7

42. Reese S. *Theorie Und Numerik Des Stabilitätsverhaltens Hyperelastischer Festkörper*. PhD thesis. TH Darmstadt, Darmstadt; 1994.

43. de Souza Neto EA, Perić D, Huang GC, Owen DRJ. Remarks on the Stability of Enhanced Strain Elements in Finite Elasticity and Elastoplasticity. *Commun. Numer. Meth. Engng.* 1995; 11(11): 951-961. doi: 10.1002/cnm.1640111109

44. Reese S. On a Physically Stabilized One Point Finite Element Formulation for Three-Dimensional Finite Elasto-Plasticity. *Comput. Methods Appl. Mech. Engrg.* 2005; 194(45): 4685-4715. doi: 10.1016/j.cma.2004.12.012

45. Areias PMA, Sá dJMAC, António CACa, Fernandes AA. Analysis of 3D Problems Using a New Enhanced Strain Hexahedral Element. *International Journal for Numerical Methods in Engineering* 2003; 58(11): 1637-1682. doi: 10.1002/nme.835

46. Simo JC, Taylor RL, Pister KS. Variational and Projection Methods for the Volume Constraint in Finite Deformation Elasto-Plasticity. *Comput. Methods Appl. Mech. Engrg.* 1985; 51(1): 177-208. doi: 10.1016/0045-7825(85)90033-7

47. Flanagan DP, Belytschko T. A Uniform Strain Hexahedron and Quadrilateral with Orthogonal Hourglass Control. *Int. J. Numer. Meth. Engng.* 1981; 17(5): 679-706. doi: 10.1002/nme.1620170504

48. Moita GF. *Non-Linear Finite Element Analysis of Continua with Emphasis on Hyperelasticity*. PhD thesis. Imperial College, London; 1994.

49. Fontes Valente RA, Alves de Sousa RJ, Natal Jorge RM. An Enhanced Strain 3D Element for Large Deformation Elastoplastic Thin-Shell Applications. *Computational Mechanics* 2004; 34(1): 38-52. doi: 10.1007/s00466-004-0551-7

50. Bonet J, Wood RD. *Nonlinear Continuum Mechanics for Finite Element Analysis*. Cambridge: Cambridge University Press. 2 ed. 2008

51. Belytschko T, Ong JSJ, Liu WK, Kennedy JM. Hourglass Control in Linear and Nonlinear Problems. *Comput. Methods Appl. Mech. Engrg.* 1984; 43(3): 251-276. doi: 10.1016/0045-7825(84)90067-7

52. Belytschko T, Bindeman LP. Assumed Strain Stabilization of the Eight Node Hexahedral Element. *Comput. Methods Appl. Mech. Engrg.* 1993; 105(2): 225-260. doi: 10.1016/0045-7825(93)90124-G

53. Schwer LE, Key SW, Pučik TA, Pu TA, Bindeman LP. An Assessment of the LS-DYNA Hourglass Formulations via the 3D Patch Test. In: *Proc. 5th European LS-DYNA Users Conference*; 2005; Birmingham.

54. Taylor RL, Simo JC, Zienkiewicz OC, Chan ACH. The Patch Test—a Condition for Assessing FEM Convergence. *Int. J. Numer. Meth. Engng.* 1986; 22(1): 39–62. doi: 10.1002/nme.1620220105

55. Zienkiewicz OC, Taylor RL, Zhu J. *The Finite Element Method. Vol. 1: Its Basis and Fundamentals*. Amsterdam: Elsevier Butterworth-Heinemann. 6 ed. 2010

56. Bonet J, Gil AJ, Ortigosa R. A Computational Framework for Polyconvex Large Strain Elasticity. *Comput. Methods Appl. Mech. Engrg.* 2015; 283: 1061-1094. doi: 10.1016/j.cma.2014.10.002

57. MacNeal RH, Harder RL. A Proposed Standard Set of Problems to Test Finite Element Accuracy. *Finite Elements in Analysis and Design* 1985; 1(1): 3-20. doi: 10.1016/0168-874X(85)90003-4

58. Puso MA. A Highly Efficient Enhanced Assumed Strain Physically Stabilized Hexahedral Element. *Int. J. Numer. Meth. Engng.* 2000; 49(8): 1029-1064. doi: 10.1002/1097-0207(20001120)49:8<1029::AID-NME990>3.0.CO;2-3

59. Simo JC. Algorithms for Static and Dynamic Multiplicative Plasticity That Preserve the Classical Return Mapping Schemes of the Infinitesimal Theory. *Comput. Methods Appl. Mech. Engrg.* 1992; 99(1): 61-112. doi: 10.1016/0045-7825(92)90123-2

60. Andelfinger U. *Untersuchungen zur Zuverlässigkeit hybrid-gemischter Finiter Elemente für Flächentragwerke*. PhD thesis. University of Stuttgart, Stuttgart; 1991.

61. Betsch P, Franke M, Janz A. Polyconvexity and the Design of Mixed Finite Elements. In: *Proc. ECCOMAS Thematic Conference on Modern Finite Element Technologies (MFET)*; 2017; Bad Honnef, Germany.

62. Betsch P, Janz A, Hesch C. A Mixed Variational Framework for the Design of Energy–Momentum Schemes Inspired by the Structure of Polyconvex Stored Energy Functions. *Comput. Methods Appl. Mech. Engrg.* 2018; 335: 660-696. doi: 10.1016/j.cma.2018.01.013

63. Schröder J, Wriggers P, Balzani D. A New Mixed Finite Element Based on Different Approximations of the Minors of Deformation Tensors. *Comput. Methods Appl. Mech. Engrg.* 2011; 200(49-52): 3583-3600. doi: 10.1016/j.cma.2011.08.009

64. Gonzalez O, Stuart AM. *A First Course in Continuum Mechanics*. Cambridge: Cambridge University Press . 2008